https://doi.org/10.5194/egusphere-2026-5329
Preprint. Discussion started: 23 September 2026

A temperature-conditioned spatial-temporal storm generator with evolving convective cell life cycles

Chien-Yu Tseng[1], Li-Pen Wang[1,2], and Christian Onof[2]

[1]Department of Civil Engineering, National Taiwan University, Taipei, 106319, Taiwan

[2]Department of Civil and Environmental Engineering, Imperial College London, London, SW7 2AZ, United Kingdom

Correspondence: Chien-Yu Tseng (cy12tseng@caece.net) and Li-Pen Wang (lpwang@ntu.edu.tw)

Abstract. Convective rainfall varies at multiple scales: individual cells evolve within storms, while the population of cell intensities can differ substantially between storms. Existing object-based stochastic storm generators commonly represent cell occurrence and movement but provide limited representation of these two sources of variability. This study develops a spatial-temporal convective storm generator that explicitly represents both. At the cell scale, radar-derived tracks are represented using three lifespan-based classes, ranging from complete growth-peak-decay lifecycles to short-lived and transient cells, with dependence among evolving intensity and geometric properties preserved using copulas. At the storm scale, each event is assigned a storm-specific distribution of cell intensities. Its location and spread are modelled using Generalised Additive Models for Location, Scale and Shape (GAMLSS), with near-surface air temperature representing systematic environmental dependence and event-level random effects representing residual storm-to-storm variability. The framework was calibrated using 169 warm-season convective storms observed over Birmingham, UK, between 2005 and 2017. The resulting generator reproduces the observed cell-property distributions, dependence structures, storm-scale organisation and temporal clustering. Importantly, using a single pooled cell-intensity distribution largely removes the observed between-storm intensity variability, whereas the storm-specific formulation recovers the observed variance partition while retaining within-storm dispersion. This improves the distributions of event-maximum cell intensity and substantially improves their extreme-value behaviour, with observed return levels remaining within the 5-95% simulation intervals across return periods of 2-100 years. The resulting framework links storm-scale environmental variability to populations of dynamically evolving convective cells, providing a computationally efficient basis for large-ensemble spatial-temporal rainfall generation and future climate-conditioned applications.

1 Introduction

Climate change is altering the frequency and intensity of weather extremes (Trenberth et al., 2003; Liu et al., 2009; Guhathakurta et al., 2011), with growing evidence of intensifying localised, short-duration rainfall associated with severe convective systems (Guerreiro et al., 2018; Fowler et al., 2021b, a; Lenderink et al., 2021). For rapidly responding urban catchments, hydrological response depends not only on rainfall magnitude but also on where intense rainfall occurs and how its spatial structure moves and evolves over time (Ochoa-Rodriguez et al., 2015; Muñoz Lopez et al., 2023). Convection-permitting (CP) models have increasingly been used to improve the simulation of such extreme precipitation (Trapp et al., 2019; Coppola et al., 2020; Prein

https://doi.org/10.5194/egusphere-2026-5329
Preprint. Discussion started: 23 September 2026

et al., 2020; Halladay et al., 2023; Archer et al., 2024). Their computational demands, however, constrain the production of the large ensembles required for hydrological risk assessment (Kendon et al., 2021; Lucas-Picher et al., 2021).

Stochastic rainfall and weather generators provide a computationally efficient means of producing high-resolution rainfall simulations. These generators are generally calibrated using historical observations from the area of interest and are designed to reproduce selected regional rainfall characteristics. Their relatively low computational cost allows them to generate long synthetic records or large ensembles, and they have therefore been widely applied to urban drainage design (Willems, 2001; Thorndahl and Andersen, 2021) and flood-risk assessment (Simões et al., 2015; Diederen and Liu, 2020; Wright et al., 2020).

Substantial progress has been made in developing stochastic generators that reproduce the space–time organisation of rainfall. Point-process models represent storms and their constituent cells as discrete objects within a hierarchical clustering structure (Rodriguez-Iturbe et al., 1987, 1988; Northrop, 2024). Initially developed for rainfall time series (Cowpertwait, 1994; Onof and Wheater, 1994, 1993), these models were later extended to space–time rainfall using dense rain-gauge networks (Wheater et al., 2000; Willems, 2001; Koutsoyiannis et al., 2003; Burton et al., 2008; Segond and Onof, 2009) and radar-derived rain-cell properties (Féral et al., 2003; Luini and Capsoni, 2011; McRobie et al., 2013; Muñoz Lopez et al., 2023). Correlated random-field generators instead simulate continuous rainfall fields designed to preserve observed dependence across spatial and temporal scales (Ferraris et al., 2003; Paschalis et al., 2013; Benoit et al., 2018; Wilcox et al., 2021; Papalexiou et al., 2021; Green et al., 2024; Schertzer and Lovejoy, 1987; Gires et al., 2020). Point-process models explicitly represent individual storms and cells, whereas random-field models preserve multiscale rainfall structure without necessarily tracking individual cells. For applications dominated by localised, short-duration convective rainfall, representing rainfall as individual cells is particularly useful because their spatial structure, movement and lifecycle evolution can be modelled explicitly.

Convective rainfall varies across several related scales. Individual cells grow, reach peak intensity and decay within a storm, while the characteristics of the cell population can differ substantially from one storm to another (Northrop, 2024; Rigo and Carmen Llasat, 2016; Kaczmarska et al., 2014; Onof and Wang, 2020; Tseng et al., 2025). A convective-storm generator should therefore represent both the evolution of cells within storms and differences between storms. Random-field generators such as STREAP (Paschalis et al., 2013) and AWE-GEN-2d (Peleg et al., 2017) draw event-specific areal rainfall properties and can therefore represent variations in storm intensity without resolving individual cells. More generally, conditioning rainfall characteristics on atmospheric covariates or discrete weather regimes allows rainfall properties to vary between environmental states (Wilks and Wilby, 1999; Ivanov et al., 2007; Jones et al., 2010; Fatichi et al., 2011; Peleg and Morin, 2014; Papalexiou, 2018) and can support internally consistent scenarios for impact and climate assessments (Sparks et al., 2018; Ahn, 2020; Van De Velde et al., 2023). For a cell-resolving generator, the challenge is to represent how cell properties evolve together over individual lifecycles while also allowing the population of cell intensities to differ between storms.

Object-based generators have improved the representation of cell occurrence, movement and spatial structure, but their treatment of cell evolution remains rather limited. Such generators commonly represent cell occurrence and advection while holding cell properties fixed throughout their lifetimes (Féral et al., 2003; Luini and Capsoni, 2011; McRobie et al., 2013; Muñoz Lopez et al., 2023). Other spatial storm generators allow selected properties to change through prescribed functions, such as a triangular-plus-tail intensity profile (Wilcox et al., 2021) or an exponential size–intensity relation (Ghirardin et al.,

https://doi.org/10.5194/egusphere-2026-5329
Preprint. Discussion started: 23 September 2026

2016). These formulations represent temporal changes in individual properties, but the joint evolution and dependence of multiple properties over the growth–peak–decay lifecycle remain partly characterised (Rigo and Carmen Llasat, 2016). This omission can lead to unrealistic rainfall extremes and hydrological responses (Muñoz Lopez et al., 2023). To address this limitation at the cell scale, Tseng et al. (2025) developed a copula-based framework that preserves both the temporal profile of cell evolution and the dependence among cell properties. That framework provides the cell-scale foundation for the present study.

A second limitation arises at the storm scale. Even when individual cell lifecycles are represented, the distribution of cell intensities can vary substantially from one storm to another. The object-based generator of McRobie et al. (2013) provides a useful illustration. Its initial formulation sampled cell-peak intensities independently from a Generalised Pareto distribution fitted to cells pooled across all observed storms, which led to too few intense storm events. The authors therefore introduced a heuristic dependence mechanism that increased the probability of generating several intense cells within the same storm. This recognised that cell intensities are organised at the storm scale, but the underlying intensity distribution remained common to all storms. The mechanism therefore strengthened the association among cell intensities within a storm without allowing the cell-intensity distribution itself to differ between storms.

This example highlights an important distinction between the organisation of cell intensities within a storm and differences in the intensity distributions of separate storms. Increasing the probability that several intense cells occur together can strengthen the internal organisation of a storm, but it does not make the population of cell intensities storm-specific. When all storms draw cells from one common intensity distribution, differences among storms are suppressed even if selected lower-order rainfall statistics are reproduced. This matters for extremes because a storm maximum arises from the collective intensities of the cells within that storm, and its simulated behaviour is sensitive to the assumed cell-intensity distribution (Onof and Wang, 2020; Marani and Ignaccolo, 2015; Marra et al., 2019). A cell-resolving generator should therefore allow different storms to draw from different cell-intensity populations rather than assigning the same parent distribution to every storm.

Representing these differences between storms then raises the question of how much of the variation can be related to the storm environment. Near-surface temperature is a suitable covariate because it is associated with systematic changes in short-duration convective rainfall intensity (Lenderink et al., 2021; Fowler et al., 2021a) and is readily available from reanalysis and climate-model output. Relating part of the variation to temperature improves the physical interpretation of the generator and provides a route towards climate-conditioned rainfall scenarios. Temperature, however, describes only one aspect of the storm environment, and storms occurring at similar temperatures can still contain different populations of cell intensities. These remaining storm-to-storm differences should be represented at the storm scale rather than treated as independent cell-level variability.

Existing generators account for parts of this variability through storm-varying mean intensity (Kaczmarska et al., 2014; Onof and Wang, 2020), weather-type-specific intensity distributions (Peleg and Morin, 2014), or temperature-dependent parameters at monthly or climatic scales (Kaczmarska et al., 2015). In the cell-resolving approaches considered here, however, temperature-related changes and the remaining differences among individual storms are not represented jointly. Moreover, differences between storms may affect not only the average cell intensity but also the spread of intensities within each storm. A

https://doi.org/10.5194/egusphere-2026-5329
Preprint. Discussion started: 23 September 2026

mechanism is therefore needed that allows both the average and spread of cell intensities to vary systematically with temperature while retaining storm-to-storm differences that temperature does not explain.

Together, these limitations motivate an object-based spatial storm generator that represents convective rainfall at two complementary levels. At the cell scale, evolving lifecycles describe how cell intensity and size change over the duration of each cell. At the storm scale, temperature and residual storm-to-storm variability define a storm-specific population of cell intensities. The proposed framework therefore links storm-scale environmental conditions to populations of dynamically evolving cells, which are subsequently rendered as two-dimensional rainfall fields. In doing so, it addresses both within-storm evolution and between-storm variability within a unified stochastic storm-generation framework.

This paper is organised as follows. Section 2 describes the pilot domain, rainfall data, storm-event selection, and the derived cell-property dataset used for model calibration. Section 3 presents the complete event-to-cell storm-generation framework, including the temperature-conditioned cell-intensity component and the reconstruction of two-dimensional rainfall fields. Section 4 evaluates the generated storms in terms of cell-scale properties, storm-scale behaviour, temporal structure, intensity variability, and extremes. Finally, Section 5 summarises the main findings and discusses future extensions towards multi-site applications.

2 Study Area and Data

2.1 Pilot domain

The pilot site is the 431 km^2 Minworth catchment in the West Midlands, England (Fig. 1, right), a highly urbanised area encompassing Birmingham and part of the Black Country. Minworth was selected because of its history of surface-water flooding associated with localised, high-intensity summer convective storms (Birmingham City Council, 2015).

Centred at the Minworth catchment, two domains with different sizes were used for storm-cell tracking and subsequent statistical analysis. These domains are:

- The **tracking domain** is a 500 km $\times$ 500 km domain centred on Minworth (the square outlined by the black dashed line in Fig. 1, left). Storm tracking was conducted over this larger domain to support reliable estimation of storm motion (Wang et al., 2015).
- The **analysis domain** is a 250 km $\times$ 250 km domain centred on Minworth. This smaller domain has denser radar coverage and hence better data quality (Fig. 1, left), while also reducing boundary effects on the extracted cell properties. Storm cells may only partially enter the tracking domain during an event period, and including these incomplete tracks in the statistical analysis may bias the estimated distributions of cell properties.

https://doi.org/10.5194/egusphere-2026-5329
Preprint. Discussion started: 23 September 2026

2.2 Datasets

2.2.1 Radar rainfall data

Radar QPEs were obtained from the British Atmospheric Data Centre as the UK Met Office Nimrod quality-controlled multi-radar composite (Golding, 1998). The product has spatial and temporal resolutions of 1 km and 5 min, respectively, and incorporates corrections for anomalous propagation, attenuation and the vertical reflectivity profile, together with an hourly nationwide mean-field bias adjustment (Harrison et al., 2000, 2009; Sandford, 2015). Its coverage over the tracking and analysis domains is shown in Fig. 1.

2.2.2 Near-surface air temperature

Hourly 2 m air temperature was obtained from the ERA5-Land reanalysis at its native $0.1°$ grid spacing (Muñoz-Sabater et al., 2021). For each radar event, the hourly temperature field was first averaged over the approximately 250 km $\times$ 250 km extraction domain centred on the pilot site. The event window was extended to whole hours by rounding its start down and its end up to the nearest hour, and the maximum of the resulting hourly spatial means was retained as the event-level covariate T_e. ERA5-Land temperatures were retrieved in kelvin and converted to degrees Celsius for model fitting and reporting.

2.3 Storm-event selection

The event catalogue was compiled using criteria informed by the WaPUG guideline for urban-drainage model verification (Gooch, 2009). Events were required to produce effective rainfall greater than 0 mm, while strict gauge-based exclusions were relaxed to retain localised storms that could otherwise be omitted. The catalogue was restricted to the convective season of May–July. Of the 171 tracked events, two did not contain full-lifecycle paths and were excluded because they could not support the common three-type calibration. The resulting calibration cohort therefore comprised 169 storm events observed between 2005 and 2017 (on average, 13 events per year).

Radar observations from the selected events were subsequently analysed using the storm-cell tracking framework of Tseng et al. (2025), from which the storm- and cell-scale properties required for calibrating the proposed storm generator were derived.

https://doi.org/10.5194/egusphere-2026-5329
Preprint. Discussion started: 23 September 2026

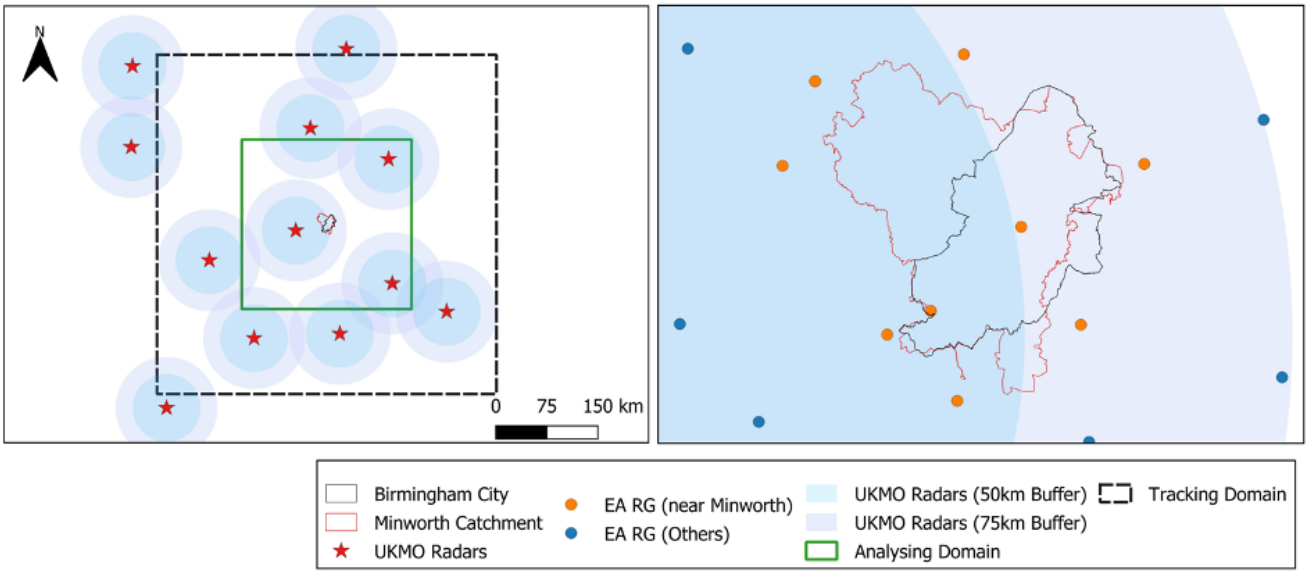

Figure 1. Pilot catchment, study domains and rainfall monitoring networks. Left: the Minworth catchment (in the very middle of the map), the neighbouring UKMO radar sites and their effective coverages, and the tracking and analysis domains are illustrated. Right panel: a close view of the Minworth catchment (and its relative location to the city of Birmingham), and the neighbouring Environment Agency (EA) rain gauges. Adapted from Tseng et al. (2025).

2.4 Derived storm and cell properties

2.4.1 Overview

The proposed storm generator requires information describing both individual convective cells and the storms that contain them. Cell-scale properties characterise the geometry and temporal evolution of individual cells, whereas storm-scale properties describe the overall organisation and environmental conditions associated with each storm event.

Cell-peak intensities were retained only when they exceeded the radar cell-extraction floor imposed by the tracking procedure. Because this floor is part of the observation process rather than the generator itself, it is treated later as a conditioning threshold in the GAMLSS fitting stage.

The required properties were derived from the radar cell tracks of Tseng et al. (2025), applied to the warm-season events selected in this study. At cell scale, the extracted properties comprise a path-specific reflectivity-derived intensity, the major and minor axis lengths $(S_{\mathrm{maj}}, S_{\mathrm{min}})$, the orientation Θ_c, the lifespan, and the per-step growth and decay rates of intensity and axis lengths. At storm scale, the derived properties include the total cell count, event duration, storm advection statistics, and the event-maximum 2 m air temperature obtained from ERA5-Land. The radar-based derivation of individual cell properties follows Tseng et al. (2025); here we focus on how these properties are organised and summarised for calibrating the storm generator.

2.4.2 Lifespan-based cell classes

Cell longevity provides a physically interpretable axis along which to represent the heterogeneity of the tracked cell population. In the observed tracks, longer-lived cells are systematically stronger and larger: mean peak intensity, major-axis length and area all increase monotonically with path duration, while path length is positively associated with peak intensity (Spearman $\rho = 0.52$). This gradient suggests that observed lifespan reflects the degree to which a cell develops and persists, rather than simply acting as a bookkeeping variable.

We therefore use lifespan to partition the 102,296 extracted cell paths into three representations. The 27,730 **full-lifecycle paths** comprise tracks of at least three 5-min observations for which the lifecycle extraction of Tseng et al. (2025) identifies a growth-peak-decay sequence. The remaining paths comprise 19,252 **two-time-step short-lived paths**, for which only one transition is observed, and 55,314 **single-time-step transient paths**, for which no temporal transition can be resolved in 5-min radar data.

In the remainder of the paper, these three classes are referred to as full-lifecycle, two-time-step short-lived and single-time-step transient paths. For compact notation in equations and tables, these classes are denoted PL1 for single-time-step transient paths, PL2 for two-time-step short-lived paths and PL3 for full-lifecycle paths.

These classes discretise a continuous longevity-vigour gradient rather than representing distinct convective regimes, because observed lifespan is inferred from radar tracking and may also be influenced by cell splitting, merging and finite observation. Separate representations are nevertheless required because different lifecycle information is available for each class: growth and decay can both be resolved for full lifecycles, only a single transition is available for two-time-step paths, and only instantaneous properties are available for single-time-step paths.

2.4.3 Advection statistics

For each eligible tracked lifecycle, the translation speed and direction were calculated from the displacement between its weighted centroids at the first and last observations. Translation speed was obtained by dividing this displacement by the elapsed time, $5(n-1)$ min for a lifecycle comprising n observations. The pooled lifecycle-speed distribution was used to calibrate the steady event velocity V_s.

Within each observed event, lifecycle directions were grouped into 5° bins, and the centre of the most frequent bin was taken as the dominant storm direction Θ_s. Directional variability was represented by the circular standard deviation. These storm-scale advection statistics subsequently constrain the generation of cells within each simulated storm (Sect. 3.2.3).

2.4.4 Calibration dataset

The complete calibration cohort described above was used for model calibration and subsequent descriptive evaluation. Because the objective of this study is to develop and characterise a stochastic storm generator rather than evaluate predictive performance, no independent temporal holdout period was reserved.

https://doi.org/10.5194/egusphere-2026-5329
Preprint. Discussion started: 23 September 2026

3 Methodology

3.1 Overview

Figure 2 provides an overview of the proposed stochastic storm generator. The framework follows the event-to-cell philosophy of object-based storm generators, in which storms are represented as collections of individual convective cells before being reconstructed into two-dimensional rainfall fields. Variability is represented at two complementary levels. At the cell scale, the generator incorporates the lifespan-based cell-path representations derived from radar observations and the lifecycle framework of Tseng et al. (2025). At the storm scale, each event is assigned its own cell-intensity distribution, whose characteristics depend partly on near-surface temperature while retaining additional storm-to-storm variability not explained by temperature.

The generation proceeds sequentially from storm events to rainfall fields. Storm occurrence and event-scale characteristics, including storm duration, cell-path count, composition and advection, are generated first. Individual cell paths are then placed within each storm and assigned their reference-state intensity, geometric and temporal-evolution properties. For each path type, the reference-state intensity is drawn from the storm-specific intensity distribution, while the remaining cell properties and their dependence follow the calibrated cell-property and lifecycle models. Finally, the evolving cells are transformed into successive two-dimensional rainfall fields using a parametric rain-cell model.

The framework combines point processes for storm occurrence and cell arrivals, probability distributions for individual storm and cell properties, and copulas for preserving dependence among jointly varying properties. The following subsections describe the event-to-cell generation procedure, cell-property and lifecycle generation, storm-specific cell-intensity modelling, rainfall-field rendering, and model calibration.

3.2 Event-to-cell storm-generation framework

The event-to-cell component determines the occurrence, composition, temporal placement and movement of the cell paths constituting each synthetic storm. Storm occurrence and event-scale properties are generated first, followed by the allocation of the total cell-path count among the lifespan-based classes (PL1, PL2 and PL3) defined in Sect. 2.4. Reference times and trajectories are then assigned to individual paths before their properties and temporal evolution are generated in Sect. 3.3.

3.2.1 Storm occurrence and event-scale properties

The storm-scale step defines the temporal envelope and common advection properties of each synthetic event. Storm arrivals are represented by a homogeneous Poisson process with rate λ_s, estimated from the observed number of events over the calibration period. For a target simulation horizon of T warm seasons, the number of storms is generated as

$$N_s \sim \mathrm{Poisson}(\lambda_s T). \qquad (1)$$

The simulated events inherit the seasonal scope of the calibration catalogue, which covers May-July for the Birmingham pilot; no additional within-year placement model is therefore applied. For each synthetic event e', the storm duration $D_{e'}$ and total

https://doi.org/10.5194/egusphere-2026-5329
Preprint. Discussion started: 23 September 2026

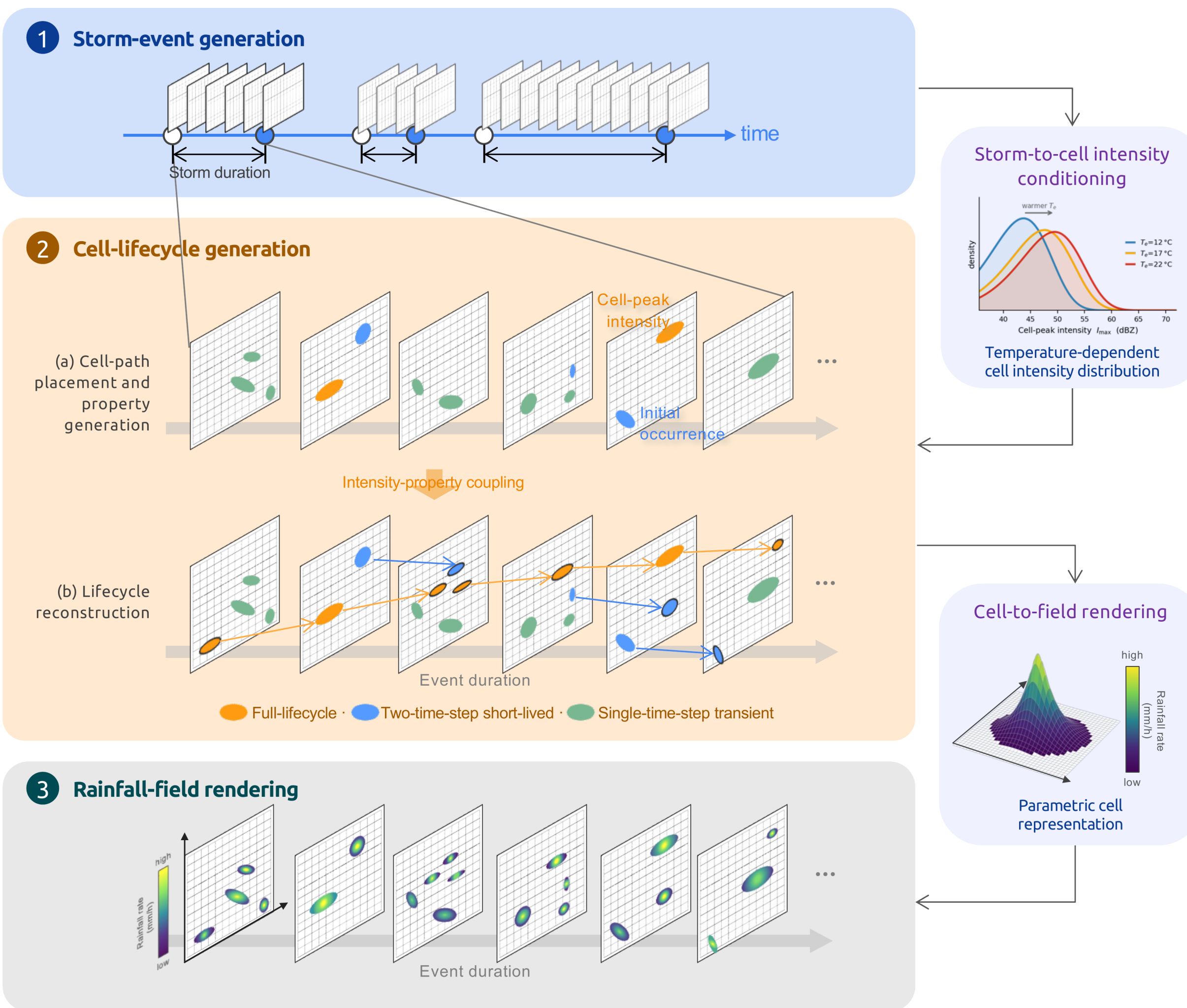

Figure 2. Conceptual overview of the proposed convective storm generator. Event-scale storms condition cell-path placement and type-specific property generation through temperature-dependent storm-to-cell distributions of reference-state intensity; reconstructed lifecycles are then rendered as successive 5-min rainfall-rate fields using a parametric cell representation. Colours denote the three lifespan-based cell-path types.

number of cell paths $N_{c,e'}$ are sampled jointly from a fitted bivariate copula. This preserves the observed positive association between event duration and cell-path count while allowing the two quantities to retain their separately fitted marginal distributions.

A steady translation speed $V_{s,e'}$ and dominant direction $\Theta_{s,e'}$ are then generated for each event. These event-scale advection properties define the common movement around which the trajectories of the constituent cell paths are generated.

https://doi.org/10.5194/egusphere-2026-5329
Preprint. Discussion started: 23 September 2026

3.2.2 Cell-path allocation and temporal placement

After the total number of cell paths has been generated, the paths are allocated among the three lifespan-based classes defined in Sect. 2.4. Because the three type proportions are constrained to be positive and sum to one, two additive log-ratios are modelled and subsequently transformed back to the original proportions. Taking the PL2 proportion as the reference, for each synthetic event we draw

$$\mathbf{y}_{e'} = \begin{pmatrix} \log(p_{e',\mathrm{PL3}}/p_{e',\mathrm{PL2}}) \\ \log(p_{e',\mathrm{PL1}}/p_{e',\mathrm{PL2}}) \end{pmatrix} \sim \mathcal{N}(\boldsymbol{\mu}_{\mathrm{ALR}}, \boldsymbol{\Sigma}_{\mathrm{ALR}}). \tag{2}$$

The proportions are recovered by the corresponding softmax transformation, so that they are positive and sum to one. Given these proportions, integer cell-path counts are drawn jointly as

$$(n_{e',\mathrm{PL3}}, n_{e',\mathrm{PL1}}, n_{e',\mathrm{PL2}}) \sim \mathrm{Multinomial}\left(N_{c,e'}, p_{e',\mathrm{PL3}}, p_{e',\mathrm{PL1}}, p_{e',\mathrm{PL2}}\right). \tag{3}$$

For enhanced readability, the noise-deconvolved ALR parameters and validation of the resulting composition are reported in Supplement S2.

Given the allocated counts, the temporal placement of cell paths within the storm is represented at the 5-min radar time step. For each cell-path type k, the number of new reference-time arrivals per time step follows a negative-binomial marginal, accommodating the observed overdispersion in cell-path arrivals. Temporal dependence is introduced through independent latent Gaussian AR(1) processes, one per cell-path type: each latent sequence is mapped through the normal CDF and subsequently through the negative-binomial inverse CDF, following the use of temporally dependent point processes in stochastic rainfall generators (Onof and Wang, 2020). A common autoregressive parameter $\phi = 0.55$ is shared across the three per-type processes and calibrated against the lag-1 autocorrelation of the aggregate active-cell sequence, rather than fitted separately for each path type.

The reference time corresponds to the characteristic peak for PL3 paths and to the initial occurrence for PL1 and PL2 paths. The resulting reference-time series determines the temporal placement of the cell paths subsequently generated in Sect. 3.3.

3.2.3 Cell-path movement

The event-level advection properties are translated into individual cell-path trajectories by combining the common storm speed with path-specific directional deviations. All cell paths within an event inherit the steady translation speed $V_{s,e'}$, while their directions vary around the dominant storm direction $\Theta_{s,e'}$. For cell path j, the directional deviation $\Delta\Theta_j$ is sampled from a von Mises distribution, which accounts for the circular nature of directional data:

$$f(\Delta\Theta_j \mid 0, \kappa) = \frac{1}{2\pi I_0(\kappa)} \exp[\kappa \cos(\Delta\Theta_j)], \tag{4}$$

https://doi.org/10.5194/egusphere-2026-5329
Preprint. Discussion started: 23 September 2026

where $I_0(\cdot)$ is the modified Bessel function of the first kind of order zero and κ controls the concentration around the event-level direction. The resulting cell-path direction is

$$\Theta_{c,j} = \Theta_{s,e'} + \Delta\Theta_j. \tag{5}$$

The initial spatial location of each path is sampled relative to the storm centre from a fitted bivariate normal distribution describing the observed spatial clustering of cells within storms. Together, the initial location, translation speed and movement direction define the trajectory along which the generated cell states are subsequently rendered.

3.3 Cell-property and lifecycle generation

Once a cell path has been allocated and assigned a reference time within a storm (Sect. 3.2), its intensity is obtained from the storm-specific cell-intensity distribution described in Sect. 3.4. This intensity is then coupled with the remaining cell properties through the type-specific joint models, yielding the property vector required for lifecycle reconstruction. The formulation follows the lifecycle framework of Tseng et al. (2025), with the intensity marginal modified in the present study to account for between-storm variability (Sect. 3.4).

For cell path j of type k, let $\mathbf{z}_{j,k}$ denote the set of properties required to reconstruct the cell states at the temporal resolution available for that path type:

$$\mathbf{z}_{j,k} = \begin{cases} \left(I_{\mathrm{ref},j,1}, S_{j,\mathrm{maj}}, S_{j,\mathrm{min}}\right), & k=1, \\ \left(I_{\mathrm{ref},j,2}, S_{j,\mathrm{ini,maj}}, S_{j,\mathrm{ini,min}}, R_{I,j}, R_{S,j}^{\mathrm{maj}}, R_{S,j}^{\mathrm{min}}\right), & k=2, \\ \left(I_{\mathrm{ref},j,3}, S_{j,\mathrm{pk,maj}}, S_{j,\mathrm{pk,min}}, L_j, R_{I,j}^{\uparrow}, R_{I,j}^{\downarrow}, R_{S,j}^{\uparrow}, R_{S,j}^{\downarrow}\right), & k=3, \end{cases} \tag{6}$$

where $k=1$, 2 and 3 denote PL1, PL2 and PL3, respectively; $I_{\mathrm{ref},j,k}$ denotes the intensity associated with the reference state of cell path j of type k, corresponding to the single represented intensity for PL1, the initial intensity for PL2 and the peak intensity for PL3; S_{maj} and S_{min} are the major and minor axis lengths, L is lifecycle duration, and R denotes the corresponding per-step rates of change. In particular, $R_{I,j}$ denotes the per-step rate of change of cell intensity, while $R_{S,j}^{\mathrm{maj}}$ and $R_{S,j}^{\mathrm{min}}$ denote the corresponding per-step rates of change of the major and minor axis lengths; for PL3, the superscripts $\uparrow$ and $\downarrow$ distinguish growth and decay. The state representation is therefore restricted to properties that can be resolved for each path class rather than imposing a common lifecycle structure on all cells.

The components of $\mathbf{z}_{j,k}$ are generated jointly using type-specific copula models so that the dependence among cell intensity, geometry, duration and rates of change is represented in the joint generation. For PL3, the peak intensity, peak axis lengths and lifecycle duration form the characteristic state, with additional joint models describing the growth and decay rates of intensity and geometry. For PL2, the initial intensity and geometry are generated together with the single resolved transition, whereas PL1 requires only the instantaneous intensity and geometry. The marginal distributions and copula specifications used for these joint models are described in Sect. 3.6.

https://doi.org/10.5194/egusphere-2026-5329
Preprint. Discussion started: 23 September 2026

The sampled properties are converted into a sequence of time-varying cell states through the type-specific reconstruction operator

$$\mathbf{x}_{j,k}(t) = \mathcal{R}_k(\mathbf{z}_{j,k})\,. \tag{7}$$

For PL3, $\mathcal{R}_k$ reconstructs the growth and decay of intensity and geometry around the generated peak state over the sampled lifecycle duration. For PL2, it reconstructs the single transition from the generated initial state, while for PL1 the generated state is retained directly. The resulting $\mathbf{x}_{j,k}(t)$ provides the intensity and geometry of each cell at every represented time step and is subsequently passed to the rainfall-field renderer in Sect. 3.5.

The reference-state intensity entering these joint models is treated differently from the other cell properties. Rather than sampling $I_{\mathrm{ref},j,k}$ from the fixed type-specific marginal used in the original lifecycle framework, the full generator replaces this marginal with a storm-specific marginal conditioned on near-surface temperature and residual storm-to-storm variability. Section 3.4 describes this component and how the resulting intensities are integrated with the existing copula-based lifecycle model.

3.4 Storm-specific cell-intensity distributions

Section 3.3 describes how the intensity and geometric properties of individual cell paths are generated while preserving their dependence. One component requires a different treatment: the marginal distribution of reference-state intensity $I_{\mathrm{ref},j,k}$. Rather than using a single type-specific intensity distribution pooled across all storms, the proposed generator allows this distribution to vary from one storm to another. The storm-specific formulation described below represents both systematic temperature dependence and remaining storm-to-storm variability, while retaining the cell-property dependence structure described in Sect. 3.3.

3.4.1 Modelling requirements

Analysis of the calibration events shows that the distribution of cell intensity varies systematically between storms. Across the three cell-path types, event-level intensity characteristics vary with the event-maximum 2 m air temperature T_e, supporting the use of temperature as a storm-scale covariate. Importantly, the variation is not restricted to the average intensity: the within-event spread also changes among storms. Moreover, substantial differences remain among events occurring at similar temperatures, indicating that temperature alone does not describe the full storm environment. The supporting exploratory analyses are shown in Fig. 3 and Supplement S4.

These observations define three requirements for the conditional intensity model. First, the centre of the cell-intensity distribution should vary with temperature. Second, its within-storm spread should also be allowed to vary. Third, individual storms should retain departures from the temperature-dependent relationship. We therefore model both the location and scale of the cell-intensity distribution as functions of temperature, with event-level random effects representing the remaining storm-to-storm variability.

https://doi.org/10.5194/egusphere-2026-5329
Preprint. Discussion started: 23 September 2026

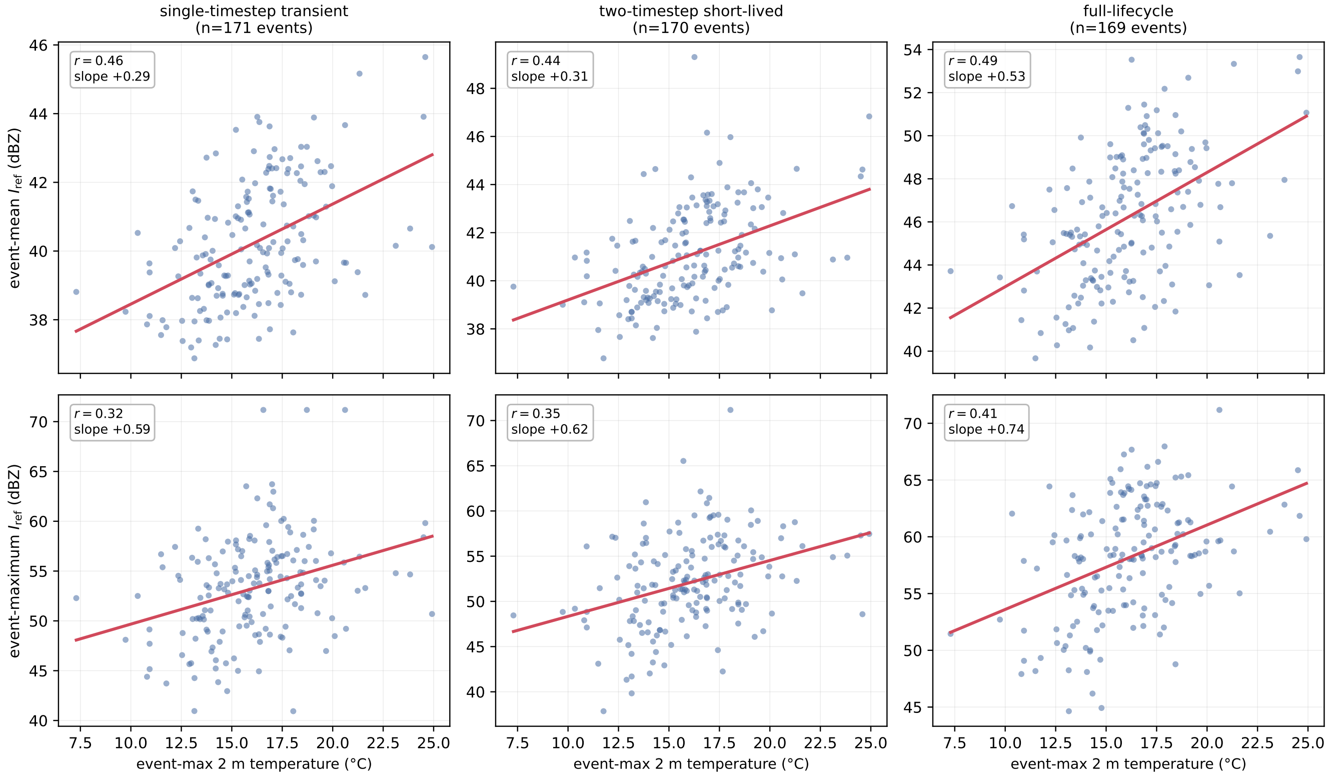

Figure 3. Relationship between event-level reference-state intensity characteristics and event-maximum 2 m air temperature for the three cell-path types. Columns show single-time-step transient, two-time-step short-lived and full-lifecycle paths; the top row shows the event mean of I_{ref}, and the bottom row shows the within-event maximum of I_{ref}.

3.4.2 Conditional intensity model

The storm-specific intensity distributions are represented using Generalised Additive Models for Location, Scale and Shape (GAMLSS). GAMLSS allows multiple parameters of a response distribution, rather than only its mean, to depend on explanatory variables and random effects. This framework has been used in hydrology for non-stationary flood-frequency and runoff analyses, where distributional parameters vary with time or climate covariates (Villarini et al., 2009; Debele et al., 2017; Scala et al., 2022). Here, it is used to describe how the distribution of reference-state intensity changes with the storm-scale environment.

For event e and cell-path type k, the reference-state intensity of cell path c is modelled as

$$I_{\mathrm{ref},c,k}^{(e)} \sim D_k(\mu_{e,k}, \sigma_{e,k}), \qquad g_{\mu,k}(\mu_{e,k}) = f_k^{\mu}(T_e) + \gamma_e^{\mu}, \qquad g_{\sigma,k}(\sigma_{e,k}) = f_k^{\sigma}(T_e) + \gamma_e^{\sigma}, \tag{8}$$

https://doi.org/10.5194/egusphere-2026-5329
Preprint. Discussion started: 23 September 2026

where D_k is the selected intensity distribution for cell-path type k; $\mu_{e,k}$ and $\sigma_{e,k}$ describe its location and scale, respectively; and $g_{\mu,k}$ and $g_{\sigma,k}$ are the corresponding link functions. The smooth functions $f_k^{\mu}(T_e)$ and $f_k^{\sigma}(T_e)$ represent systematic temperature dependence, while γ_e^{μ} and γ_e^{σ} represent residual event-level deviations. The latter are modelled jointly so that storm-to-storm deviations in intensity level and spread can remain correlated.

Because the radar cell extraction imposes a lower intensity threshold T_k, the model is fitted and sampled conditional on exceeding this threshold. Accordingly, the conditional density used for cell generation is

$$f_{k,\mathrm{tr}}(x \mid \mu_{e,k}, \sigma_{e,k}, T_k) = \frac{f_k(x \mid \mu_{e,k}, \sigma_{e,k})}{1 - F_k(T_k \mid \mu_{e,k}, \sigma_{e,k})}, \qquad x > T_k, \tag{9}$$

where f_k and F_k denote the density and cumulative distribution functions of D_k, respectively. The selected response families, link functions, temperature smooths and random-effect structures are described in Sect. 3.6.

3.4.3 Integration with the cell-property sampler

For each simulated storm e', a storm-specific cell-intensity distribution is generated for each cell-path type. The event temperature $T_{e'}$ is first assigned. For simulations representing the Birmingham calibration climate, $T_{e'}$ is sampled from the fitted marginal distribution of the observed event-level temperature covariate; in climate-conditioned applications it can instead be supplied by the driving climate data. A correlated pair of event-level random effects, $(\gamma_{e'}^{\mu}, \gamma_{e'}^{\sigma})$, is then drawn from the fitted type-specific covariance structure and combined with $T_{e'}$ through Eq. (8). The required number of reference-state intensities is subsequently sampled from the resulting truncated storm-specific distribution.

These intensities replace the fixed reference-state intensity marginal used by the type-specific cell-property models in Sect. 3.3, while their dependence on the remaining cell properties is retained through the copula structure. This intensity–property coupling is implemented differently for the three path types, but follows a common integration pattern: the sampled intensities are rank-matched to the copula-generated order and used to condition the remaining lifecycle properties through the corresponding type-specific copula component. For PL1 and PL2, the rank-matched intensities are inserted into the path-specific copula records, and the remaining lifecycle properties are generated conditionally before reconstruction. For PL3, peak intensity, peak geometry and lifecycle duration are generated through the conditional inverse-Rosenblatt construction used by the lifecycle model, with the resulting lifecycle duration determining the cell's temporal extent around the reference time. The resulting cell records are then reconstructed through the type-specific lifecycle representations of Sect. 3.3; the common integration pattern is detailed in Supplement S1.

3.5 Rainfall-field rendering

After the cell paths have been generated and their time-varying properties reconstructed, the final step converts the individual cell states into two-dimensional rainfall fields. Each reconstructed cell is represented by an elliptical exponential field of the EXCELL family (Capsoni and Luini, 2009; Féral et al., 2003). This functional form is consistent with the volume-normalised mean radial profile of the Birmingham radar cells (Supplement S6) and with previous analyses of convective-cell profiles (von

https://doi.org/10.5194/egusphere-2026-5329
Preprint. Discussion started: 23 September 2026

Hardenberg et al., 2003; Rebora and Ferraris, 2006). The full derivation, parameter calibration and numerical implementation of the renderer are provided in Supplement S6.

A scale adjustment is required before the generated cell properties can be used in the continuous rainfall field. The intensity component of each reconstructed cell state is converted from dBZ to rainfall rate using the standard Marshall–Palmer Z–R relation (Marshall and Palmer, 1948). Because the radar observations have 1 km grid support, the resulting intensity represents the mean rainfall intensity of the radar grid cell containing the observed maximum rather than an underlying point-scale maximum. Similarly, the generated major and minor axes correspond to moment-based measures of the spatial dispersion of the tracked radar cell and are not directly equivalent to the decay scales of a continuous exponential field. The renderer therefore accounts explicitly for these differences in observational scale and geometrical representation.

Three geometrical quantities are distinguished. The tracking procedure provides moment semi-axes ($S_{\mathrm{maj}}^{\mathrm{mom}}, S_{\mathrm{min}}^{\mathrm{mom}}$), which describe the spatial dispersion of the tracked cell. The spatial extent of the otherwise unbounded exponential field is defined by its threshold footprint, comprising the 1 km grid cells with rainfall rate at or above $I_{\mathrm{thr}} = 5.6\,\mathrm{mm\,h^{-1}}$. This rendering threshold is distinct from the dBZ extraction thresholds used for fitting the cell-intensity distributions in Sect. 3.4. Finally, the continuous EXCELL field is characterised by exponential decay scales. These quantities are related statistically rather than treated as interchangeable descriptions of cell size.

Writing A_{obs} for the observed threshold-footprint area, the mapping between the moment geometry and an area-equivalent threshold geometry is described by

$$R = \frac{\pi S_{\mathrm{maj}}^{\mathrm{mom}} S_{\mathrm{min}}^{\mathrm{mom}}}{A_{\mathrm{obs}}}, \qquad \left(\widetilde{S}_{\mathrm{maj}}, \widetilde{S}_{\mathrm{min}}\right) = \frac{\left(S_{\mathrm{maj}}^{\mathrm{mom}}, S_{\mathrm{min}}^{\mathrm{mom}}\right)}{\sqrt{R}}. \tag{10}$$

The ratio R is calibrated separately for each cell-path type and sampled during simulation. The transformation preserves the generated cell orientation and aspect ratio while mapping the moment-based geometry to a threshold footprint consistent with the observed cell area.

For the resulting geometry, the continuous peak-time rainfall field is written as

$$I_{\mathrm{peak}}(x,y) = I_{\mathrm{thr}} \exp[L\{1-\rho(x,y)\}], \tag{11}$$

where $\rho(x,y)$ is the dimensionless elliptical distance from the cell centre and L determines the underlying point-scale peak, $I_{\mathrm{max},p} = I_{\mathrm{thr}}\exp(L)$. Following the finite-resolution peak-inversion principle of Tseng et al. (2025), L is determined so that aggregation of the continuous field to the 1 km radar grid reproduces the generated grid-scale peak intensity. Together with the sampled R, this determines the point-scale peak and spatial decay scales while remaining consistent with both the generated radar-scale peak and the calibrated threshold-footprint geometry. Details of the observation operator and numerical solution are given in Supplement. S6.

The procedure is applied independently to every reconstructed cell state and translated and rotated according to its generated position and orientation. Where multiple cells overlap, the grid-cell rainfall intensity is taken as the maximum of the contributing cell fields, consistent with the representation used in the radar-based cell extraction. Repeating the procedure at successive

https://doi.org/10.5194/egusphere-2026-5329
Preprint. Discussion started: 23 September 2026

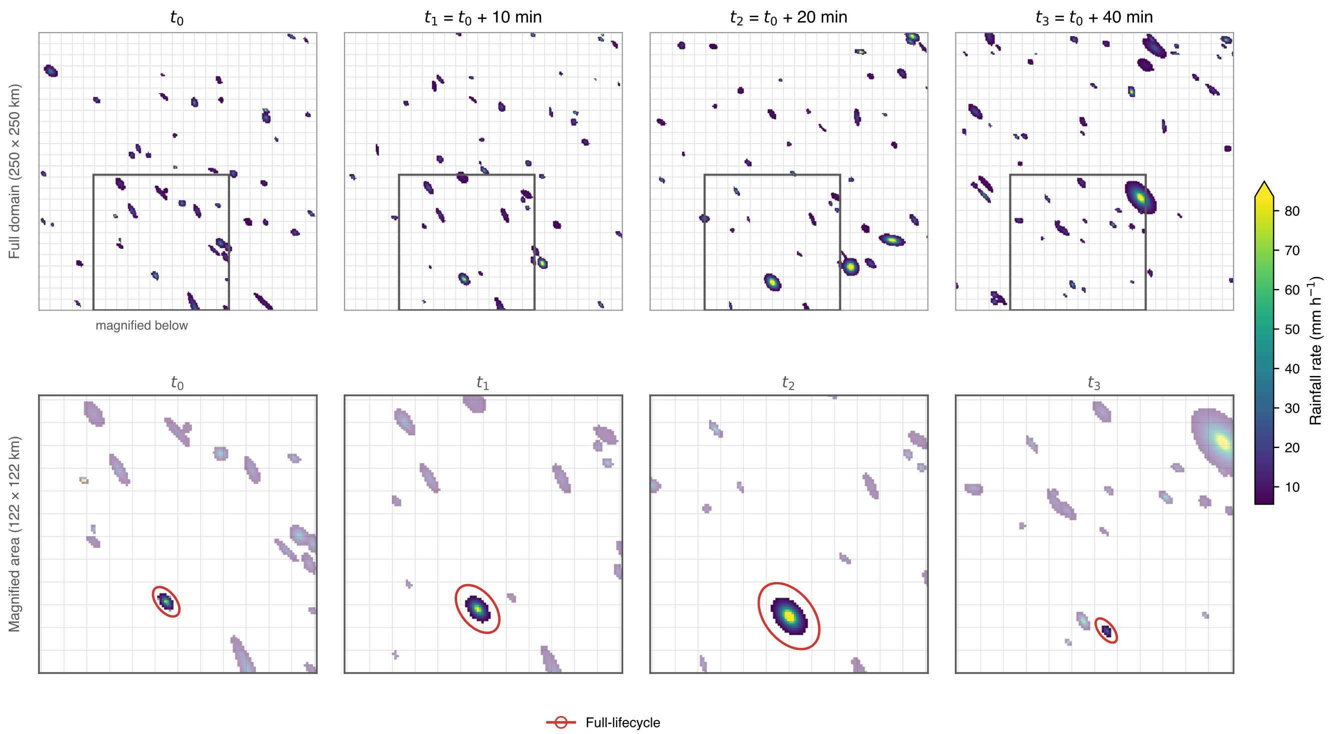

Figure 4. Illustrative rainfall-rate fields from four 5-min snapshots of one synthetic storm generated by the production scale-consistent theoretical renderer. All panels use the same spatial window and colour scale. The figure illustrates the event-to-field output of the generator and is not a spatial-skill validation.

5-min time steps produces the complete spatial-temporal rainfall field for each synthetic storm. Figure 4 shows an illustrative example of the resulting rainfall-rate fields.

3.6 Model fitting and calibration

The statistical components introduced in Sections 3.2- 3.5 were calibrated using the complete 2005–2017 storm cohort described in Sect. 2. The fitting procedure separates the marginal behaviour of individual storm and cell properties from their dependence structure. The storm-specific cell-intensity component requires a separate distributional-regression fit because its marginal distribution varies between events. This section summarises the calibration procedures and selected model specifications; numerical parameter values and additional fitting diagnostics are reported in the Supplement.

3.6.1 Marginal distributions and dependence models

For the event-to-cell and lifecycle components, marginal distributions were fitted separately to the relevant storm- and cell-scale quantities. Candidate parametric families were estimated by maximum likelihood, with the preferred family selected

https://doi.org/10.5194/egusphere-2026-5329
Preprint. Discussion started: 23 September 2026

using the Akaike information criterion (AIC). Where no candidate parametric family provided an adequate representation, an empirical distribution was retained. For each cell-path type, a common copula representation was used across the observed storm cohort to describe how the cell properties vary together. This common representation is used for joint cell generation, while the storm-specific formulation introduced in Sect. 3.4 allows the cell-intensity distribution itself to vary between events. Candidate Gaussian, Archimedean and vine copulas were evaluated using AIC together with their ability to reproduce the corresponding cell-level Kendall τ values.

At storm scale, this procedure was applied to event duration and total cell-path count and their joint dependence. At cell scale, separate cell-property models were used for the properties available for PL1, PL2 and PL3, reflecting the different life-cycle information resolved for each path type. The type-specific copula models describe the dependence among cell intensity, geometry, duration and rates of change used in Sect. 3.3. Cell-path arrivals and movement were calibrated separately using the negative-binomial–AR(1) and von Mises models, respectively, as described in Sect. 3.2.

Table 1 summarises the selected marginal and dependence models. The reference-state intensity entry in the table represents the base marginal used in fitting the cell-property dependence structure; during storm generation it is replaced by the storm-specific intensity distribution described in Sect. 3.4. Representative marginal goodness-of-fit diagnostics are provided in Supplement S1.

Table 1. Selected marginal and dependence models for the event-to-cell and cell-property components. The base I_{ref} marginals are used to calibrate the type-specific cell-property dependence models; during storm generation they are replaced by the storm-specific distributions described in Sect. 3.4. Numerical parameter values are reported in the Supplement.

Stage	Quantity	Selected model
Storm event	Inter-storm arrivals	Poisson rate λ_s
	Storm duration D_E	Log-normal
	Cell-path count per event N_c	Gamma
	(D_E, N_c) joint dependence	Bivariate copula C_E
Cell path	Cell-path-type composition	Noise-deconvolved ALR-normal + multinomial
	Reference-time arrivals	Negative binomial + Gaussian-copula AR(1)
	Directional deviation $\Delta\Theta$	von Mises
Cell property	PL3 characteristic state	Vine copula
	PL3 growth/decay rates ($\times 3$ variables)	3D vine copula each
	PL1 characteristic state	Vine copula
	PL2 characteristic state + rates	Vine copula
	Base I_{ref} marginal	Shifted Weibull (PL3); shifted log-normal (PL1, PL2)
	Axes / growth–decay-rate marginals	Log-logistic, Weibull, Gamma, Beta (PL3); log-normal (PL1); log-logistic (PL2)

https://doi.org/10.5194/egusphere-2026-5329
Preprint. Discussion started: 23 September 2026

3.6.2 Storm-specific intensity model

The GAMLSS component of Sect. 3.4 was fitted separately for each cell-path type while pooling cells across events. Event-level random effects were included on both the location and scale predictors, allowing individual events to retain deviations in intensity level and within-event spread while sharing information in the estimation of the overall temperature response. The fitted covariance between the two random effects subsequently provides the storm-to-storm variability used when generating new events.

For each path type, event-maximum temperature T_e enters the location and scale predictors through penalised B-splines. The production fits use a shifted log-normal family for PL1 and PL2 and the Weibull type 3 formulation (WEI3) for PL3. The location parameter uses an identity link for the shifted log-normal models and a log link for the Weibull model, while the scale parameter uses a log link throughout. All families are fitted conditional on the corresponding radar cell-extraction threshold described in Sect. 2.2.1.

The interpretation of the scale-related parameter is family-specific. For the shifted log-normal family, σ is the standard deviation on the log-intensity scale, such that larger values correspond to greater within-event spread. For the Weibull type 3 formulation, σ is the shape parameter and larger values correspond to a narrower distribution. Accordingly, the fitted σ–temperature relationships should be interpreted in terms of the corresponding response family rather than compared directly across path types.

The models were fitted by penalised maximum likelihood using the `gamlss` R package (Stasinopoulos and Rigby, 2007). Penalisation controls unnecessary complexity in the temperature-response curves, with smoothness selected using the Fellner–Schall procedure. The penalty on the event-level scale effect was fixed at $\lambda_\sigma = 1$ to avoid excessive shrinkage of storm-to-storm variability in within-event spread. Candidate response families were evaluated separately for each path type using convergence, parameter stability and residual diagnostics under the same truncated-likelihood and random-effect structure. AIC and the Schwarz Bayesian criterion (SBC) were used for within-type comparisons only and were not compared across path types. Detailed family-selection and fitting diagnostics are provided in Supplement. S1. Table 2 summarises the production specification used for simulation, including the response family, parameter predictors and links, extraction threshold, and fitted association between the event-level location and scale deviations.

Table 2. Production specification of the storm-specific cell-intensity model for each cell-path type. T denotes event-maximum 2 m air temperature, $\mathrm{pb}(T)$ a penalised B-spline temperature term, and "RE" an event-level random effect. The final column gives the fitted correlation between the event-level location and scale deviations after accounting for temperature.

Cell-path type	Family $f_{0,k}$	μ: predictor/link	σ: predictor/link	T_k (dBZ)	$r(\gamma^\mu, \gamma^\sigma)$
PL1	LOGNOtr	$\mathrm{pb}(T) + \mathrm{RE}$ / identity	$\mathrm{pb}(T) + \mathrm{RE}$ / log	34.586	-0.085
PL2	LOGNOtr	$\mathrm{pb}(T) + \mathrm{RE}$ / identity	$\mathrm{pb}(T) + \mathrm{RE}$ / log	34.367	$+0.132$
PL3	WEI3tr	$\mathrm{pb}(T) + \mathrm{RE}$ / log	$\mathrm{pb}(T) + \mathrm{RE}$ / log	35.528	$+0.554$

https://doi.org/10.5194/egusphere-2026-5329
Preprint. Discussion started: 23 September 2026

4 Results and discussion

4.1 Evaluation design and metrics

The evaluation broadly follows the sequence in which the generator assembles a storm. We first examine the reproduction of cell- and storm-scale properties and their dependence, followed by the temporal organisation of cell paths within storms. We then assess whether the storm-specific intensity formulation reproduces the observed between-storm variability and event-maximum intensity distributions, before evaluating the consequences for extreme-value behaviour using the SMEV (Simplified Meta-statistical Extreme Value) approach (Marani and Ignaccolo, 2015; Marra et al., 2019) as an independent downstream check.

Marginal distributions are compared using the Perkins Skill Score (PSS) (Perkins et al., 2007), dependence using Kendall's rank correlation, and temporal organisation using the lag-1 autocorrelation and the Perkins Skill Scores of the reference-time arrival and active-count distributions. The storm-specific intensity formulation is assessed through temperature-intensity relationships, the partition of cell-intensity variance between and within storms, and within-event dispersion. The production ensemble comprises 100 13-year simulations generated using parameters calibrated for the Birmingham pilot[1]. For finite-sample diagnostics, each ensemble member has the same duration as the observed record, allowing the spread across members to represent the sampling variability expected for a record of this length.

For two binned distributions, the Perkins Skill Score is calculated as

$$\mathrm{PSS} = \sum_{i=1}^{n} \min(Z_{\mathrm{sim},i}, Z_{\mathrm{obs},i}), \tag{12}$$

where $Z_{\mathrm{sim},i}$ and $Z_{\mathrm{obs},i}$ are the normalised frequencies in bin i. The score ranges from zero to one, with larger values indicating greater overlap between the simulated and observed distributions. Kendall's τ is used as a non-parametric measure of rank dependence, while the lag-1 autocorrelation and the Perkins Skill Scores of the reference-time arrival and active-count distributions are evaluated for the within-storm cell-path sequences.

Two additional quantities are used to summarise the extreme-value and between-storm evaluations. For cell-path type k and return period T, the simulated-to-observed return-level ratio and its percentage form are defined as

$$Q_k(T) = \frac{\overline{RL}_{k,\mathrm{sim}}(T)}{RL_{k,\mathrm{obs}}(T)}, \qquad B_k(T) = 100\,[Q_k(T) - 1]. \tag{13}$$

where $RL_{k,\mathrm{obs}}(T)$ is the observed return level and $\overline{RL}_{k,\mathrm{sim}}(T)$ is the ensemble-mean simulated return level. The lower row of the SMEV figure reports $Q_k(T)$, for which unity indicates agreement with the observations; the percentage values reported in the Supplement are $B_k(T)$, for which zero indicates agreement. For the storm-level variance decomposition, the fraction of the raw cell-intensity variance attributable to differences between storms is

[1] The ensemble size $N = 100$ provides a combined simulation length of $N \times N_{\mathrm{years}} = 1300$ yr, exceeding ten times the longest return period considered.

https://doi.org/10.5194/egusphere-2026-5329
Preprint. Discussion started: 23 September 2026

$$f_{\text{between}} = \frac{SS_{\text{between}}}{SS_{\text{between}} + SS_{\text{within}}}, \tag{14}$$

where SS_{between} and SS_{within} denote the between- and within-storm sums of squares, respectively.

4.2 Representation of cell-property distributions and dependence

Figure 5 summarises the marginal distributions of the cell properties resolved by the three path representations, using PSS values calculated for the observation-sized production members. Across the displayed properties, PSS values range from 0.82 to 0.95. The transient cell-intensity distribution has the lowest score (0.82), although the scores for cell intensity remain above 0.80 for all three path representations. The geometric and intensity-related properties and the full-lifecycle rates generally show closer agreement. The fitted marginal distributions underlying these comparisons are illustrated in the Supplement S1.

Figure 6 evaluates the pairwise rank dependence among reference-state-intensity and geometry-related properties using Kendall's τ, calculated from cells pooled across storms for both the observations and each production member. The observed dependence patterns are generally reproduced by the production ensemble, with the most noticeable departures occurring for some relationships involving reference-state intensity. Each production member represents the same 13-year period as the observations, while its numbers of storms and cells are generated by the model; the ensemble spread therefore represents realisation-to-realisation variability for records of comparable duration.

Supplement S5 extends this comparison to the lifecycle variables, including peak-rate associations, the three full-lifecycle path-length relationships, and all fifteen pairwise relationships represented by the six-dimensional copula for two-time-step paths. These additional diagnostics show similarly close agreement overall, with some departures for individual lifecycle relationships. Taken together, the results indicate that the generator reproduces the evaluated cell-property distributions and captures the main pairwise dependence patterns required to reconstruct evolving cell paths.

https://doi.org/10.5194/egusphere-2026-5329
Preprint. Discussion started: 23 September 2026

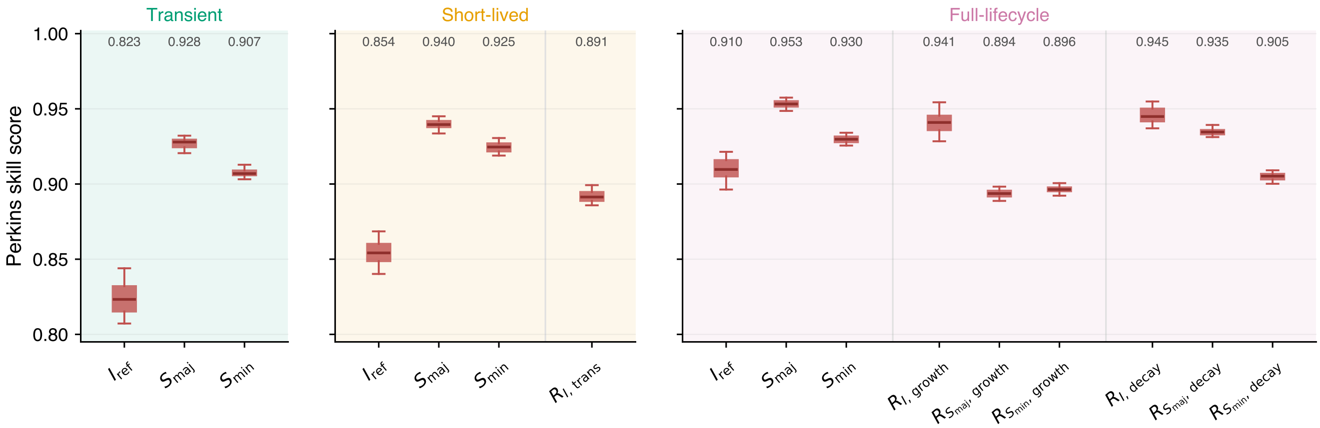

Figure 5. Perkins Skill Scores (PSS) for cell-property marginal distributions across the production ensemble. The panels show single-time-step transient (PL1), two-time-step short-lived (PL2) and full-lifecycle (PL3) paths. Scores are calculated for the observation-sized production members.

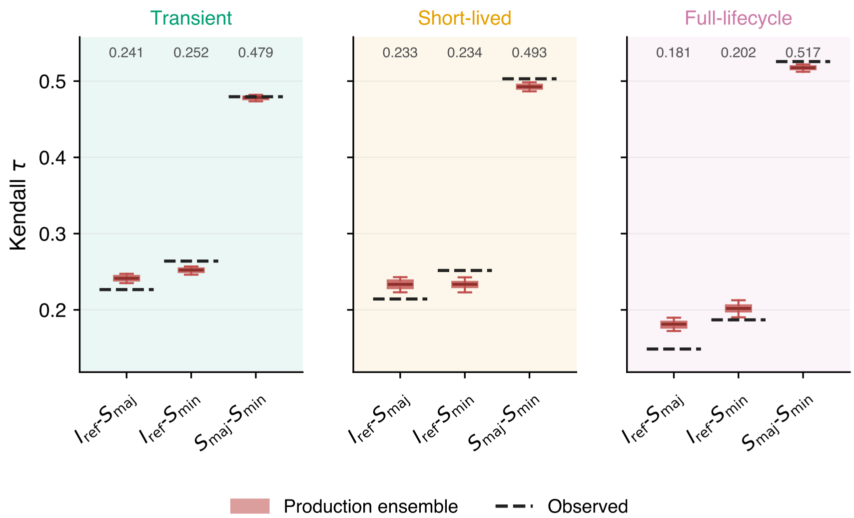

Figure 6. Reference-state-property rank dependence in the production ensemble, calculated using cells pooled across storms. Each ensemble distribution contains one Kendall's τ value computed from all the cells of each of 100 production members, that is, one value per 13-year realisation at approximately the observed sample size; the spread therefore reflects realisation-to-realisation variability at the observed record length. Dashed lines indicate the corresponding observed values for the three I_{ref}–geometry pairs of each cell-path type.

https://doi.org/10.5194/egusphere-2026-5329
Preprint. Discussion started: 23 September 2026

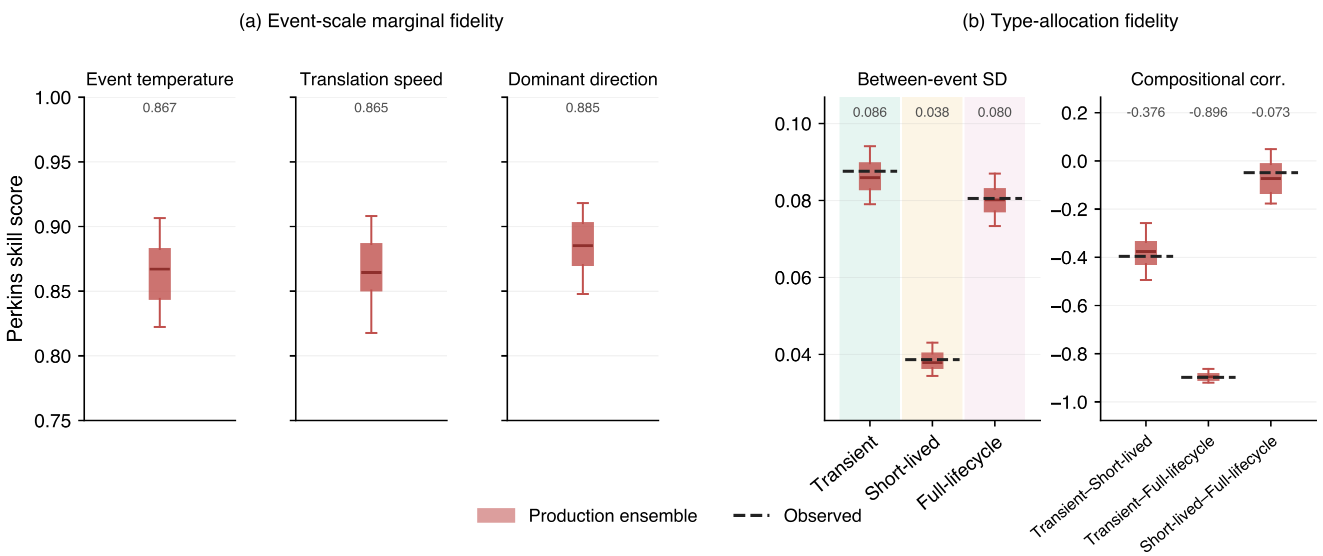

Figure 7. Event-scale characteristics and path-type composition in the production ensemble. Panel (a) shows Perkins Skill Scores for event-maximum 2 m temperature, translation speed and dominant direction. Panel (b) compares the between-storm standard deviations of the three path-type proportions and their pairwise compositional correlations with the observed values (dashed lines).

4.3 Storm-scale organisation and temporal clustering

Storm-scale organisation is evaluated in terms of both event-level characteristics and the temporal organisation of cell paths within storms. Figure 7 first compares the generated event covariates and path-type composition with the observations. The event-maximum 2 m temperature, sampled from its fitted marginal distribution (Sect. 3.6.2), gives a PSS of approximately 0.87 against the observed ERA5 event temperatures. Similar scores are obtained for storm translation speed and dominant direction, indicating that the generated event-scale conditions are consistent with their observed distributions.

The dependence between event duration and total cell-path count is also retained by the event-scale copula, with the full comparison provided in Supplement S2. Figure 7 further shows that the production ensemble reproduces the observed between-storm variability in path-type composition and the dependence among the three proportions. The event-scale PSS values range from 0.87 to 0.88, while the observed allocation summaries fall within the production-ensemble 5-95 % intervals. Together, these results indicate that the event-to-cell framework reproduces the main observed characteristics governing storm composition.

We next evaluate whether the generated cell paths reproduce the temporal clustering observed within storms. The observed reference-time arrivals occur in sustained bursts separated by relatively quiescent periods. Although an independent negative-binomial sampler can reproduce the marginal arrival-count distribution, it cannot reproduce this serial dependence. Figure 8 therefore compares the observed and generated distributions of reference-time arrival and active cell-path counts per 5-min time step. With the calibrated AR(1) dependence, the aggregate lag-1 autocorrelation closely matches the observed value

https://doi.org/10.5194/egusphere-2026-5329
Preprint. Discussion started: 23 September 2026

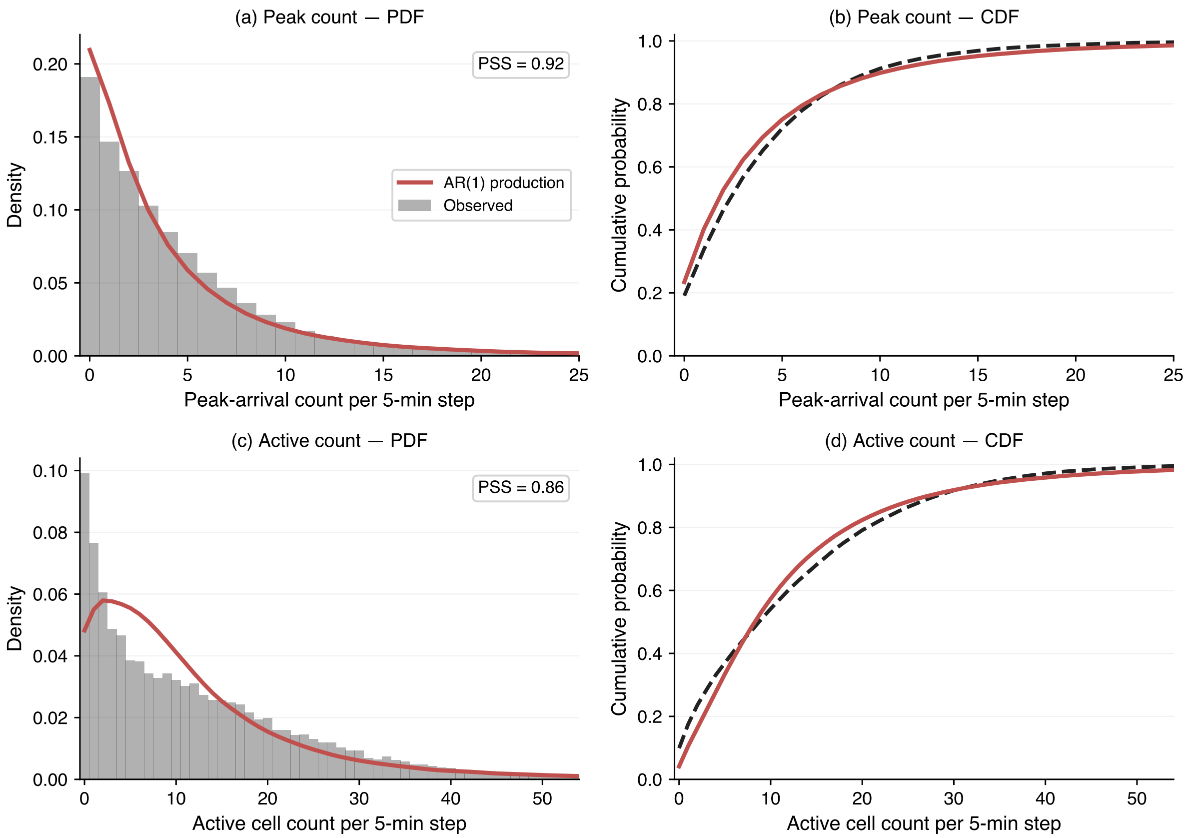

Figure 8. Evaluation of within-storm temporal clustering. Panels (a)–(d) compare the observed and production-ensemble distributions of reference-time arrival and active cell-path counts per 5-min time step; Perkins Skill Scores are annotated in the density panels. The production ensemble uses independent per-type latent Gaussian AR(1) processes with $\phi = 0.55$.

(0.393 versus 0.396), while the arrival-count distribution is well reproduced and the active-count distribution improves relative to the independent baseline. Fully quiescent intervals nevertheless remain under-represented, indicating that the model captures the dominant short-range temporal clustering but not the complete intermittency of observed cell activity. Alternative common-factor specifications are compared in Supplement S3.

4.4 Representation of between-storm intensity variability

We next assess whether the storm-specific intensity formulation reproduces the observed variation in cell-intensity populations between storms while retaining realistic variability among cells within individual storms. Figure 9 first examines the two mechanisms introduced in Sect. 3.4: systematic variation with temperature and residual storm-to-storm variability.

Figure 9 examine the temperature-related changes in event-mean intensity (left panel) and within-event spread (middle panel). Across the three cell-path types, the production ensemble reproduces the direction and approximate magnitude of the

https://doi.org/10.5194/egusphere-2026-5329
Preprint. Discussion started: 23 September 2026

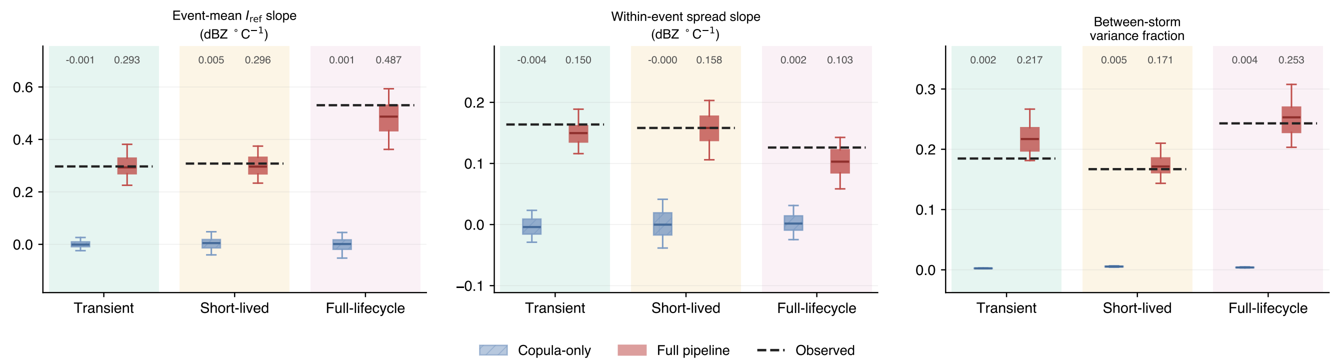

Figure 9. Temperature response and variance partition of reference-state intensity. Boxes show the copula-only baseline and full production ensembles for the three cell-path types, while dashed lines show the observed values. The panels compare temperature-related changes in event-mean I_{ref} and within-event spread, together with the fraction of total I_{ref} variance attributed to differences between storms.

observed temperature relationships, with the observed responses lying within the corresponding ensemble 5-95 % intervals. This indicates that conditioning both the location and scale of the cell-intensity distribution on temperature captures the observed systematic changes in not only the average cell intensity but also its within-storm dispersion.

The variance partition provides a stronger test of the storm-specific formulation. When cell intensities are sampled from a common distribution across storms (the copula-only baseline), very little of the total cell-intensity variance is attributed to differences between storms. In contrast, the full formulation recovers the observed between-storm contribution while retaining the within-storm dispersion across all three path types. The observed between-storm variance fractions fall within the full-ensemble 5-95 % intervals, whereas the copula-only baseline remains close to the level expected from random grouping. Thus, reproducing the marginal cell-intensity distribution alone is insufficient to reproduce the observed storm-to-storm differences; allowing the intensity population itself to vary between events is necessary. Detailed fitting diagnostics are reported in Supplement S1, and generalisation beyond the calibration events is further examined in Supplement S4.

The consequences of this variance structure are next examined through the distribution of event-maximum cell intensity. Unlike the cell-level distributions evaluated in Sect. 4.2, event maxima are not fitted directly but emerge from the generated cell-intensity population, the number of cells within each event and their storm-to-storm variation. They therefore provide an integrated diagnostic of whether these components combine to reproduce the upper part of the event-scale intensity distribution.

To quantify agreement between the simulated and observed event-maximum cell-intensity distributions without binning, the Wasserstein-1 distance is defined as

$$W_1(F_{\mathrm{sim}}, F_{\mathrm{obs}}) = \int_0^1 \left| F_{\mathrm{sim}}^{-1}(u) - F_{\mathrm{obs}}^{-1}(u) \right| \mathrm{d}u, \tag{15}$$

https://doi.org/10.5194/egusphere-2026-5329
Preprint. Discussion started: 23 September 2026

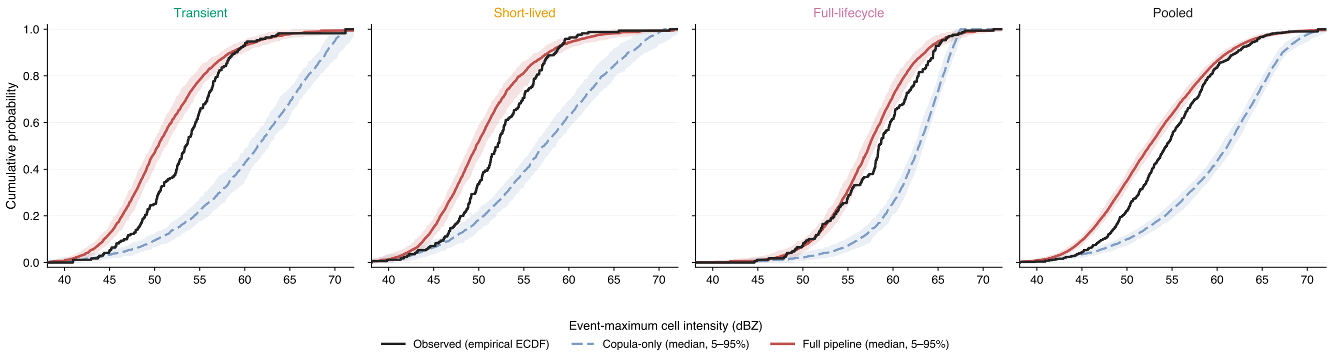

Figure 10. Event-maximum cell-intensity distributions for the three cell-path types and all paths combined. The event maxima are calculated from the path-specific reference-state intensities. Observations are shown as empirical step functions; dashed and solid curves show the copula-only baseline and full production-ensemble medians, respectively, with shaded 5-95 % ranges across 100 observation-sized members.

where F_{sim} and F_{obs} denote the empirical CDFs of the simulated and observed event-maximum cell-intensity samples, respectively, and F_{sim}^{-1} and F_{obs}^{-1} are their corresponding quantile functions. For each production member, the distance is calculated against the fixed observed sample; values are expressed in dBZ, with smaller values indicating closer agreement.

Figure 10 compares the observed event maxima with the copula-only baseline and full production ensemble for each path type and for all paths combined.

Across all three path types, the full formulation shifts the simulated event-maximum distributions towards the observations relative to the copula-only baseline. The corresponding Wasserstein-1 distances defined in Eq. (15) decrease for all three path types and for the combined sample, with numerical results reported in Supplement S4. Because event maxima integrate cell-level intensity, event cell counts and between-storm variability, this improvement cannot be attributed to the storm-specific intensity component alone. Nevertheless, together with the variance decomposition above, it shows that restoring between-storm differences in the cell-intensity population improves the representation of the upper event-scale intensity distribution. The consequences for extreme return levels are examined in Sect. 4.5.

4.5 Consequences for extreme-value behaviour

The differences in between-storm variability identified in Sect. 4.4 should ultimately affect the upper tail of event-scale cell intensity. We therefore examine whether these differences propagate to extreme return levels using the Simplified Metastatistical Extreme Value (SMEV) formulation (Marani and Ignaccolo, 2015; Marra et al., 2019). SMEV is used here as an independent downstream diagnostic: the same event definition, fitting rule, annual event rate and return-level calculation are applied to the observations, the copula-only baseline and the full production ensemble, without tuning against the resulting return-level biases.

SMEV is applied separately to the event maxima of the reference-state intensities for each path type. Let $\mathcal{C}_{e,k}$ denote the set of cell paths of type k in event e, and define $X_{e,k} = \max_{j \in \mathcal{C}_{e,k}} I_{\mathrm{ref},j,k}$. Let n_k denote the mean number of corresponding

https://doi.org/10.5194/egusphere-2026-5329
Preprint. Discussion started: 23 September 2026

events per year and F_k the fitted two-parameter Weibull CDF. The annual-maximum distribution and T-year return level are then given by

$$G_k(x) = F_k(x)^{n_k}, \qquad G_k(RL_k(T)) = 1 - \frac{1}{T}. \tag{16}$$

The same procedure is applied to the observations and each simulation member for return periods from 2 to 100 years. Because the analysis is performed directly on event-maximum cell intensities, it evaluates the extreme behaviour generated by the event-to-cell model independently of the subsequent rainfall-field rendering and spatial aggregation.

The contrast between the two generator formulations is consistent with the event-maximum distributions identified in Sect. 4.4. In the copula-only baseline, sampling cell intensities from a common distribution across storms produces event maxima with insufficient storm-to-storm dispersion. This is particularly evident for the single-time-step transient and full-lifecycle path types, for which the resulting Weibull fits have larger shape parameters and hence lighter upper tails than observed. Allowing the cell-intensity distribution to vary between storms through temperature dependence and residual event-level variability increases the dispersion of event maxima and changes both the level and return-period dependence of the resulting return levels.

Figure 11 shows the resulting SMEV return levels over 2-100 years. The copula-only baseline increasingly departs from the observed extreme-value behaviour, whereas the full production ensemble remains close to the observations across the evaluated return periods and all three cell-path types. In particular, the observed return levels remain within the full-ensemble 5-95 % interval at every evaluated return period.

The relative behaviour is shown more directly in the lower row of Fig. 11. The copula-only baseline increasingly deviates from a simulated-to-observed ratio of one, while the full production ensemble remains close to one across the three path types. Together with the variance decomposition and event-maximum distributions in Sect. 4.4, these results show that representing storm-to-storm differences in the cell-intensity population is important not only for reproducing observed event-scale variability, but also for preserving its propagation into long-return-period extremes. Detailed return-level values and sensitivity to the SMEV fitting window are reported in Supplement S4.

5 Conclusions

We have developed a stochastic convective-storm generator that represents variability at two complementary levels. At the cell level, the generator extends the lifecycle framework of Tseng et al. (2025) to represent evolving cell intensity and geometry using the lifecycle information available for each path type. At the storm level, it allows the population of cell intensities to differ between events, with both the location and spread of the distribution varying systematically with near-surface temperature while retaining residual storm-to-storm variability. These components are embedded within an event-to-cell framework that generates storm occurrence, cell-path composition, temporal clustering and advection before reconstructing the evolving cells into two-dimensional rainfall fields.

The production ensemble reproduces the principal cell-property distributions and pairwise dependence patterns, together with the storm-scale characteristics and temporal organisation observed over Birmingham. Importantly, sampling cell inten-

https://doi.org/10.5194/egusphere-2026-5329
Preprint. Discussion started: 23 September 2026

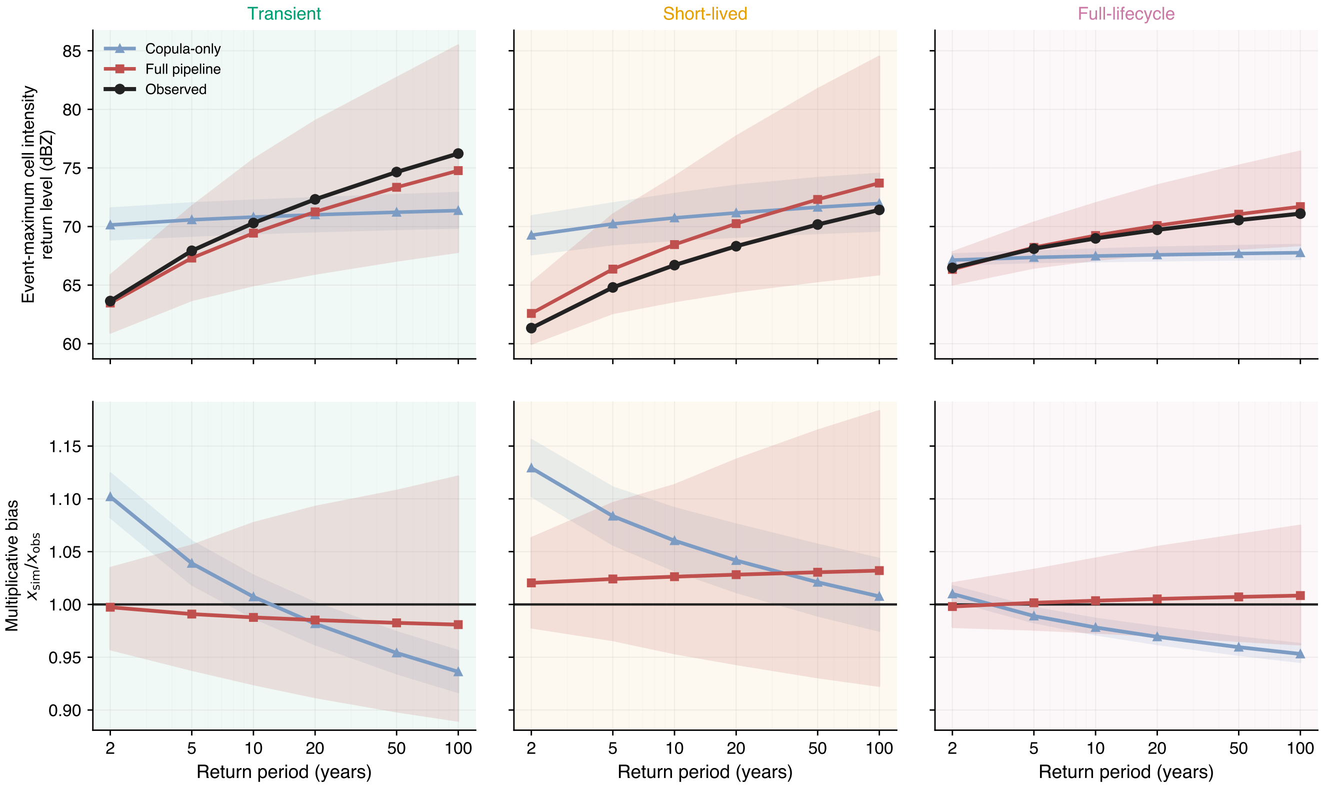

Figure 11. SMEV return levels of the event-maximum cell intensity for return periods of 2-100 years, with the event maxima calculated from the path-specific reference-state intensities. The upper row shows absolute return levels and the lower row shows the simulated-to-observed return-level ratio for the three cell-path types. Curves show ensemble means and shaded bands show the 5-95 % range across 100 observation-sized production members.

sities from a common distribution across storms substantially suppresses the observed between-storm intensity variability. Allowing the cell-intensity population itself to vary between storms recovers the observed variance partition while preserving within-storm dispersion. This improvement propagates to event maxima and their extreme-value behaviour: across return periods of 2–100 years, the full production ensemble remains close to the observed return levels for all three cell-path types, with the observations lying within the ensemble 5-95 % intervals.

Several limitations define the scope for further model development. The shifted log-normal representation of the two-time-step short-lived paths retains a small upper-tail discrepancy, which could motivate a more flexible tail representation. The current AR(1) arrival model captures the dominant short-range temporal clustering but under-represents fully quiescent intervals, suggesting that a richer representation of active and quiescent periods may be required. In addition, the cell-property copulas are common across the storm cohort and therefore do not explicitly distinguish within-storm dependence from storm-

https://doi.org/10.5194/egusphere-2026-5329
Preprint. Discussion started: 23 September 2026

to-storm differences in multivariate cell properties. A hierarchical dependence formulation could address this distinction where sufficient data are available.

The broader limitation is one of evaluation and transferability. The framework is demonstrated for a single pilot region, and although it ultimately generates two-dimensional rainfall fields, their spatial dependence, scale-dependent intermittency and hydrological response have not yet been evaluated systematically. Multi-site evaluation across contrasting hydroclimatic regimes is therefore required to establish which model components and temperature-intensity relationships are transferable. Near-surface temperature nevertheless provides a physically interpretable covariate that is readily available from reanalysis and climate-model output, while residual storm-level variability represents differences among storms that temperature alone cannot explain. Extending this conditioning to additional atmospheric covariates and testing the resulting rainfall fields across sites would provide the next steps towards climate-conditioned stochastic generation of localised convective rainfall. The proposed framework provides a computationally efficient basis for generating large ensembles of spatial–temporal convective storms while representing both the evolution of individual cells and systematic and residual differences between storm events.

Data availability. The Nimrod radar data used in this work can be accessed via CEDA (Centre for Environmental Data Analysis).

Author contributions. Chien-Yu Tseng (CT) and Li-Pen Wang (LW) co-led the conceptualisation of the study with support from Christian Onof (CO). CT led the model development and implementation with support from LW and CO. LW, CT and CO jointly designed the evaluation experiments and prepared the manuscript.

Competing interests. No competing interests are present.

Acknowledgements. The authors express their gratitude for the financial support received from two National Science and Technology Council research projects (NSTC and 113-2923-M-002-001-MY4 and 115-2625-M-002-014-). In addition, they extend their appreciation to the Centre for Environmental Data Analysis for providing access to the NIMROD radar data produced by the Met Office. Generative artificial intelligence tools were used during manuscript preparation to assist with language editing and improve the clarity of the text. The authors reviewed and take full responsibility for the final content.

https://doi.org/10.5194/egusphere-2026-5329
Preprint. Discussion started: 23 September 2026

References

Ahn, K.-H.: Coupled Annual and Daily Multivariate and Multisite Stochastic Weather Generator to Preserve Low- and High-Frequency Variability to Assess Climate Vulnerability, Journal of Hydrology, 581, 124 443, https://doi.org/10.1016/j.jhydrol.2019.124443, 2020.

Archer, L., Hatchard, S., Devitt, L., Neal, J. C., Coxon, G., Bates, P. D., Kendon, E. J., and Savage, J.: Future Change in Urban Flooding Using New Convection-Permitting Climate Projections, Water Resources Research, 60, e2023WR035 533, https://doi.org/10.1029/2023WR035533, 2024.

Benoit, L., Allard, D., and Mariethoz, G.: Stochastic Rainfall Modeling at Sub-kilometer Scale, Water Resources Research, 54, 4108–4130, https://doi.org/10.1029/2018WR022817, 2018.

Birmingham City Council: Birmingham Surface Water Management Plan, Final Report, https://www.birmingham.gov.uk/downloads/file/2561/surface_water_management_plan_for_birmingham_-_final_report, (last access: 21 September 2026), 2015.

Burton, A., Kilsby, C., Fowler, H., Cowpertwait, P., and O'Connell, P.: RainSim: A Spatial–Temporal Stochastic Rainfall Modelling System, Environmental Modelling & Software, 23, 1356–1369, https://doi.org/10.1016/j.envsoft.2008.04.003, 2008.

Capsoni, C. and Luini, L.: Analysis of spatial and temporal properties of rain cells for rainfall modeling purposes, Italian Journal of Remote Sensing / Rivista Italiana di Telerilevamento, 41, 51–62, https://doi.org/10.5721/ItJRS20094134, 2009.

Coppola, E., Sobolowski, S., Pichelli, E., Raffaele, F., Ahrens, B., Anders, I., Ban, N., Bastin, S., Belda, M., Belusic, D., et al.: A first-of-its-kind multi-model convection permitting ensemble for investigating convective phenomena over Europe and the Mediterranean, Climate Dynamics, 55, 3–34, https://doi.org/10.1007/s00382-018-4521-8, 2020.

Cowpertwait, P. S. P.: A generalized point process model for rainfall, Proceedings of the Royal Society of London. Series A: Mathematical and Physical Sciences, 447, 23–37, https://doi.org/10.1098/rspa.1994.0126, 1994.

Debele, S. E., Bogdanowicz, E., and Strupczewski, W. G.: Around and about an application of the GAMLSS package to non-stationary flood frequency analysis, Acta Geophysica, 65, 885–892, https://doi.org/10.1007/s11600-017-0072-3, 2017.

Diederen, D. and Liu, Y.: Dynamic spatio-temporal generation of large-scale synthetic gridded precipitation: with improved spatial coherence of extremes, Stochastic environmental research and risk assessment, 34, 1369–1383, https://doi.org/10.1007/s00477-019-01724-9, 2020.

Fatichi, S., Ivanov, V. Y., and Caporali, E.: Simulation of future climate scenarios with a weather generator, Advances in Water Resources, 34, 448–467, https://doi.org/10.1016/j.advwatres.2010.12.013, 2011.

Ferraris, L., Gabellani, S., Rebora, N., and Provenzale, A.: A Comparison of Stochastic Models for Spatial Rainfall Downscaling, Water Resources Research, 39, 2003WR002 504, https://doi.org/10.1029/2003WR002504, 2003.

Fowler, H. J., Lenderink, G., Prein, A. F., Westra, S., Allan, R. P., Ban, N., Barbero, R., Berg, P., Blenkinsop, S., Do, H. X., et al.: Anthropogenic intensification of short-duration rainfall extremes, Nature Reviews Earth & Environment, 2, 107–122, https://doi.org/10.1038/s43017-020-00128-6, 2021a.

Fowler, H. J., Wasko, C., and Prein, A. F.: Intensification of short-duration rainfall extremes and implications for flood risk: current state of the art and future directions, Philosophical Transactions of the Royal Society A: Mathematical, Physical and Engineering Sciences, 379, 20190 541, https://doi.org/10.1098/rsta.2019.0541, 2021b.

Féral, L., Sauvageot, H., Castanet, L., and Lemorton, J.: HYCELL—A new hybrid model of the rain horizontal distribution for propagation studies: 1. Modeling of the rain cell, Radio Science, 38, https://doi.org/10.1029/2002RS002802, 2003.

https://doi.org/10.5194/egusphere-2026-5329
Preprint. Discussion started: 23 September 2026

Ghirardin, S., Capsoni, C., and Luini, L.: Time Evolution of Synthetic Rain Cells for the Synthesis of Attenuation Time Series, in: 2016 10th European Conference on Antennas and Propagation (EuCAP), pp. 1–5, IEEE, ISBN 978-88-907018-6-3, https://doi.org/10.1109/EuCAP.2016.7481928, 2016.

Gires, A., Tchiguirinskaia, I., and Schertzer, D.: Blunt extension of discrete universal multifractal cascades: development and application to downscaling, Hydrological Sciences Journal, 65, 1204–1220, https://doi.org/10.1080/02626667.2020.1736297, 2020.

Golding, B. W.: Nimrod: A System for Generating Automated Very Short Range Forecasts, Meteorological Applications, 5, 1–16, https://doi.org/10.1017/S1350482798000577, 1998.

Gooch, M. N.: Use of Rainfall Data from Flow Surveys, WaPUG User Note No. 6., Chartered Institute of Water and Environmental Management (CIWEM), https://www.ciwem.org/assets/pdf/Special%20Interest%20Groups/Urban%20Drainage%20Group/WAPUG_User_Note_06.pdf, (last access: 21 September 2026), 2009.

Green, A. C., Kilsby, C., and Bárdossy, A.: A framework for space–time modelling of rainfall events for hydrological applications of weather radar, Journal of Hydrology, 630, 130 630, https://doi.org/10.1016/j.jhydrol.2024.130630, 2024.

Guerreiro, S. B., Fowler, H. J., Barbero, R., Westra, S., Lenderink, G., Blenkinsop, S., Lewis, E., and Li, X.-F.: Detection of continental-scale intensification of hourly rainfall extremes, Nature Climate Change, 8, 803–807, https://doi.org/10.1038/s41558-018-0245-3, 2018.

Guhathakurta, P., Sreejith, O. P., and Menon, P. A.: Impact of climate change on extreme rainfall events and flood risk in India, Journal of Earth System Science, 120, 359–373, https://doi.org/10.1007/s12040-011-0082-5, 2011.

Halladay, K., Kahana, R., Johnson, B., Still, C., Fosser, G., and Alves, L.: Convection-permitting climate simulations for South America with the Met Office Unified Model, Climate Dynamics, 61, 5247–5269, https://doi.org/10.1007/s00382-023-06853-0, 2023.

Harrison, D. L., Driscoll, S. J., and Kitchen, M.: Improving Precipitation Estimates from Weather Radar Using Quality Control and Correction Techniques, Meteorological Applications, 7, 135–144, https://doi.org/10.1017/S1350482700001468, 2000.

Harrison, D. L., Scovell, R. W., and Kitchen, M.: High-Resolution Precipitation Estimates for Hydrological Uses, Proceedings of the Institution of Civil Engineers - Water Management, 162, 125–135, https://doi.org/10.1680/wama.2009.162.2.125, 2009.

Ivanov, V. Y., Bras, R. L., and Curtis, D. C.: A weather generator for hydrological, ecological, and agricultural applications, Water resources research, 43, W10 406, https://doi.org/10.1029/2006WR005364, 2007.

Jones, P., Harpham, C., Kilsby, C., Glenis, V., and Burton, A.: UK Climate Projections science report: Projections of future daily climate for the UK from the Weather Generator, UK Climate Projections science report, https://doi.org/10.5281/zenodo.7357058, 2010.

Kaczmarska, J. M., Isham, V. S., and Onof, C.: Point process models for fine-resolution rainfall, Hydrological Sciences Journal, 59, 1972–1991, https://doi.org/10.1080/02626667.2014.925558, 2014.

Kaczmarska, J. M., Isham, V. S., and Northrop, P.: Local generalised method of moments: an application to point process-based rainfall models, Environmetrics, 26, 312–325, https://doi.org/10.1002/env.2338, 2015.

Kendon, E., Prein, A., Senior, C., and Stirling, A.: Challenges and outlook for convection-permitting climate modelling, Philosophical Transactions of the Royal Society A, 379, 20190 547, https://doi.org/10.1098/rsta.2019.0547, 2021.

Koutsoyiannis, D., Onof, C., and Wheater, H. S.: Multivariate rainfall disaggregation at a fine timescale, Water Resources Research, 39, https://doi.org/10.1029/2002WR001600, 2003.

Lenderink, G., de Vries, H., Fowler, H. J., Barbero, R., van Ulft, B., and van Meijgaard, E.: Scaling and responses of extreme hourly precipitation in three climate experiments with a convection-permitting model, Philosophical Transactions of the Royal Society A: Mathematical, Physical and Engineering Sciences, 379, 20190 544, https://doi.org/10.1098/rsta.2019.0544, 2021.

https://doi.org/10.5194/egusphere-2026-5329
Preprint. Discussion started: 23 September 2026

Liu, S. C., Fu, C., Shiu, C.-J., Chen, J.-P., and Wu, F.: Temperature dependence of global precipitation extremes, Geophysical Research Letters, 36, https://doi.org/10.1029/2009GL040218, 2009.

Lucas-Picher, P., Argüeso, D., Brisson, E., Tramblay, Y., Berg, P., Lemonsu, A., Kotlarski, S., and Caillaud, C.: Convection-permitting modeling with regional climate models: Latest developments and next steps, Wiley Interdisciplinary Reviews: Climate Change, 12, e731, https://doi.org/10.1002/wcc.731, 2021.

Luini, L. and Capsoni, C.: MultiEXCELL: A New Rain Field Model for Propagation Applications, IEEE Transactions on Antennas and Propagation, 59, 4286–4300, https://doi.org/10.1109/TAP.2011.2164175, 2011.

Marani, M. and Ignaccolo, M.: A metastatistical approach to rainfall extremes, Advances in Water Resources, 79, 121–126, https://doi.org/10.1016/j.advwatres.2015.03.001, 2015.

Marra, F., Zoccatelli, D., Armon, M., and Morin, E.: A simplified MEV formulation to model extremes emerging from multiple nonstationary underlying processes, Advances in Water Resources, 127, 280–290, https://doi.org/10.1016/j.advwatres.2019.04.002, 2019.

Marshall, J. S. and Palmer, W. M.: The Distribution of Raindrops with Size, Journal of Meteorology, 5, 165–166, https://doi.org/10.1175/1520-0469(1948)005<0165:TDORWS>2.0.CO;2, 1948.

McRobie, F. H., Wang, L.-P., Onof, C., and Kenney, S.: A spatial-temporal rainfall generator for urban drainage design, Water Science and Technology, 68, 240–249, https://doi.org/10.2166/wst.2013.241, 2013.

Muñoz-Sabater, J., Dutra, E., Agustí-Panareda, A., Albergel, C., Arduini, G., Balsamo, G., Boussetta, S., Choulga, M., Harrigan, S., Hersbach, H., Martens, B., Miralles, D. G., Piles, M., Rodríguez-Fernández, N. J., Zsoter, E., Buontempo, C., and Thépaut, J.-N.: ERA5-Land: a state-of-the-art global reanalysis dataset for land applications, Earth System Science Data, 13, 4349–4383, https://doi.org/10.5194/essd-13-4349-2021, 2021.

Muñoz Lopez, C., Wang, L.-P., and Willems, P.: Statistical characterization of rainfall fields based upon a 12-year high-resolution radar archive of Belgium, Atmospheric Research, 283, 106 544, https://doi.org/10.1016/j.atmosres.2022.106544, 2023.

Northrop, P. J.: Stochastic Models of Rainfall, Annual Review of Statistics and Its Application, 11, 51–74, https://doi.org/10.1146/annurev-statistics-040622-023838, 2024.

Ochoa-Rodriguez, S., Wang, L.-P., Gires, A., Pina, R. D., Reinoso-Rondinel, R., Bruni, G., Ichiba, A., Gaitan, S., Cristiano, E., van Assel, J., et al.: Impact of spatial and temporal resolution of rainfall inputs on urban hydrodynamic modelling outputs: A multi-catchment investigation, Journal of Hydrology, 531, 389–407, https://doi.org/10.1016/j.jhydrol.2015.05.035, 2015.

Onof, C. and Wang, L.-P.: Modelling rainfall with a Bartlett–Lewis process: new developments, Hydrology and Earth System Sciences, 24, 2791–2815, https://doi.org/10.5194/hess-24-2791-2020, 2020.

Onof, C. and Wheater, H. S.: Modelling of British rainfall using a random parameter Bartlett-Lewis Rectangular Pulse Model, Journal of Hydrology, 149, 67–95, https://doi.org/10.1016/0022-1694(93)90100-N, 1993.

Onof, C. and Wheater, H. S.: Improvements to the modelling of British rainfall using a modified Random Parameter Bartlett-Lewis Rectangular Pulse Model, Journal of Hydrology, 157, 177–195, https://doi.org/10.1016/0022-1694(94)90104-X, 1994.

Papalexiou, S. M.: Unified theory for stochastic modelling of hydroclimatic processes: Preserving marginal distributions, correlation structures, and intermittency, Advances in water resources, 115, 234–252, https://doi.org/10.1016/j.advwatres.2018.02.013, 2018.

Papalexiou, S. M., Serinaldi, F., and Porcu, E.: Advancing Space-Time Simulation of Random Fields: From Storms to Cyclones and Beyond, Water Resources Research, 57, e2020WR029 466, https://doi.org/10.1029/2020WR029466, 2021.

Paschalis, A., Molnar, P., Fatichi, S., and Burlando, P.: A stochastic model for high-resolution space-time precipitation simulation, Water Resources Research, 49, 8400–8417, https://doi.org/10.1002/2013WR014437, 2013.

Peleg, N. and Morin, E.: Stochastic convective rain-field simulation using a high-resolution synoptically conditioned weather generator (HiReS-WG), Water Resources Research, 50, 2124–2139, https://doi.org/10.1002/2013WR014836, 2014.

Peleg, N., Fatichi, S., Paschalis, A., Molnar, P., and Burlando, P.: An advanced stochastic weather generator for simulating 2-D high-resolution climate variables, Journal of Advances in Modeling Earth Systems, 9, 1595–1627, https://doi.org/10.1002/2016MS000854, 2017.

Perkins, S. E., Pitman, A. J., Holbrook, N. J., and McAneney, J.: Evaluation of the AR4 climate models' simulated daily maximum temperature, minimum temperature, and precipitation over Australia using probability density functions, Journal of Climate, 20, 4356–4376, https://doi.org/10.1175/JCLI4253.1, 2007.

Prein, A. F., Liu, C., Ikeda, K., Bullock, R., Rasmussen, R. M., Holland, G. J., and Clark, M.: Simulating North American mesoscale convective systems with a convection-permitting climate model, Climate Dynamics, 55, 95–110, https://doi.org/10.1007/s00382-017-3993-2, 2020.

Rebora, N. and Ferraris, L.: The structure of convective rain cells at mid-latitudes, Advances in Geosciences, 7, 31–35, https://doi.org/10.5194/adgeo-7-31-2006, 2006.

Rigo, T. and Carmen Llasat, M.: Forecasting hailfall using parameters for convective cells identified by radar, Atmospheric Research, 169, 366–376, https://doi.org/10.1016/j.atmosres.2015.10.021, 2016.

Rodriguez-Iturbe, I., Cox, D. R., and Isham, V.: Some models for rainfall based on stochastic point processes, Proceedings of the Royal Society of London A: Mathematical, Physical and Engineering Sciences, 410, 269–288, https://doi.org/10.1098/rspa.1987.0039, 1987.

Rodriguez-Iturbe, I., Cox, D. R., and Isham, V.: A point process model for rainfall: further developments, Proceedings of the Royal Society of London A: Mathematical, Physical and Engineering Sciences, 417, 283–298, https://doi.org/10.1098/rspa.1988.0061, 1988.

Sandford, C.: Correcting for wind drift in high resolution radar rainfall products: a feasibility study, Journal of Hydrology, 531, 284–295, https://doi.org/10.1016/j.jhydrol.2015.03.023, 2015.

Scala, P., Cipolla, G., Treppiedi, D., and Noto, L. V.: The Use of GAMLSS Framework for a Non-Stationary Frequency Analysis of Annual Runoff Data over a Mediterranean Area, Water, 14, 2848, https://doi.org/10.3390/w14182848, 2022.

Schertzer, D. and Lovejoy, S.: Physical modeling and analysis of rain and clouds by anisotropic scaling multiplicative processes, Journal of Geophysical Research: Atmospheres, 92, 9693–9714, https://doi.org/10.1029/JD092iD08p09693, 1987.

Segond, M.-L. and Onof, C.: Modelling of space–time rainfall for three UK regions, Proceedings of the Institution of Civil Engineers-Water Management, 162, 147–158, https://doi.org/10.1680/wama.2009.162.2.147, 2009.

Simões, N. E., Ochoa-Rodríguez, S., Wang, L.-P., Pina, R. D., Marques, A. S., Onof, C., and Leitão, J. P.: Stochastic Urban Pluvial Flood Hazard Maps Based upon a Spatial-Temporal Rainfall Generator, Water, 7, 3396–3406, https://doi.org/10.3390/w7073396, 2015.

Sparks, N. J., Hardwick, S. R., Schmid, M., and Toumi, R.: IMAGE: A Multivariate Multi-Site Stochastic Weather Generator for European Weather and Climate, Stochastic Environmental Research and Risk Assessment, 32, 771–784, https://doi.org/10.1007/s00477-017-1433-9, 2018.

Stasinopoulos, D. M. and Rigby, R. A.: Generalized additive models for location scale and shape (GAMLSS) in R, Journal of Statistical Software, 23, 1–46, https://doi.org/10.18637/jss.v023.i07, 2007.

Thorndahl, S. and Andersen, C. B.: CLIMACS: A method for stochastic generation of continuous climate projected point rainfall for urban drainage design, Journal of Hydrology, 602, 126 776, https://doi.org/10.1016/j.jhydrol.2021.126776, 2021.

Trapp, R. J., Hoogewind, K. A., and Lasher-Trapp, S.: Future Changes in Hail Occurrence in the United States Determined through Convection-Permitting Dynamical Downscaling, Journal of Climate, 32, 5493–5509, https://doi.org/10.1175/JCLI-D-18-0740.1, 2019.

Trenberth, K. E., Dai, A., Rasmussen, R. M., and Parsons, D. B.: The Changing Character of Precipitation, Bulletin of the American Meteorological Society, 84, 1205–1218, https://doi.org/10.1175/BAMS-84-9-1205, 2003.

Tseng, C.-Y., Wang, L.-P., and Onof, C.: Modelling Convective Cell Life Cycles with a Copula-Based Approach, Hydrology and Earth System Sciences, 29, 1–25, https://doi.org/10.5194/hess-29-1-2025, 2025.

Van De Velde, J., Demuzere, M., De Baets, B., and Verhoest, N.: Future Multivariate Weather Generation by Combining Bartlett-Lewis and Vine Copula Models, Hydrological Sciences Journal, 68, 1–15, https://doi.org/10.1080/02626667.2022.2144322, 2023.

Villarini, G., Smith, J. A., Serinaldi, F., Bales, J., Bates, P. D., and Krajewski, W. F.: Flood frequency analysis for nonstationary annual peak records in an urban drainage basin, Advances in Water Resources, 32, 1255–1266, https://doi.org/10.1016/j.advwatres.2009.05.003, 2009.

von Hardenberg, J., Ferraris, L., and Provenzale, A.: The shape of convective rain cells, Geophysical Research Letters, 30, https://doi.org/10.1029/2003GL018539, 2003.

Wang, L.-P., Ochoa-Rodríguez, S., Van Assel, J., Pina, R. D., Pessemier, M., Kroll, S., Willems, P., and Onof, C.: Enhancement of radar rainfall estimates for urban hydrology through optical flow temporal interpolation and Bayesian gauge-based adjustment, Journal of Hydrology, 531, 408–426, https://doi.org/10.1016/j.jhydrol.2015.05.049, 2015.

Wheater, H. S., Isham, V. S., Cox, D. R., Chandler, R. E., Kakou, A., Northrop, P. J., Oh, L., Onof, C., and Rodriguez-Iturbe, I.: Spatial-temporal rainfall fields: modelling and statistical aspects, Hydrology and Earth System Sciences, 4, 581–601, https://doi.org/10.5194/hess-4-581-2000, 2000.

Wilcox, C., Aly, C., Vischel, T., Panthou, G., Blanchet, J., Quantin, G., and Lebel, T.: Stochastorm: A Stochastic Rainfall Simulator for Convective Storms, Journal of Hydrometeorology, 22, 387–404, https://doi.org/10.1175/JHM-D-20-0017.1, 2021.

Wilks, D. S. and Wilby, R. L.: The weather generation game: a review of stochastic weather models, Progress in physical geography, 23, 329–357, https://doi.org/10.1177/030913339902300302, 1999.

Willems, P.: A spatial rainfall generator for small spatial scales, Journal of Hydrology, 252, 126–144, https://doi.org/10.1016/S0022-1694(01)00446-2, 2001.

Wright, D. B., Yu, G., and England, J. F.: Six decades of rainfall and flood frequency analysis using stochastic storm transposition: Review, progress, and prospects, Journal of Hydrology, 585, 124 816, https://doi.org/10.1016/j.jhydrol.2020.124816, 2020.